Synthesis of ternary NiCo-MnO_2 nanocomposite and its application as a novel high energy supercapattery device

Kabir O. Oyedotun, Moshawe J. Madito, Damilola Y. Momodu, Abdulmajid A. Mirghni, Tshifhiwa M. Masikhwa and Ncholu Manyala*

Department of Physics, Institute of Applied Materials, SARCHI Chair in Carbon Technology and Materials, University of Pretoria, Pretoria 0028, South Africa.

*Corresponding author's email: ncholu.manyala@up.ac.za, Tel.: + (27)12 420 3549.

Highlights

•NiCo/NiCoMn-mixed hydroxides, ternary NiCo-MnO_2 nanostructures were successfully synthesised.
•The samples were used as electrodes for electrochemical supercapacitor in 1 M KOH.
•The electrode materials exhibit good charge storage capability on both regions.
•Assembled NiCo-MnO_2/C-FP hybrid supercapattery displays high electrochemical performance.

ABSTRACT

NiCo /NiCoMn-mixed hydroxides and ternary NiCo-MnO_2 electrode materials were successfully synthesised by a force-driven hydrolysis of hydrated nickel, cobalt and manganese nitrate salts at 40 °C for 2 h with an additional annealing step adopted in producing the NiCo-MnO_2 sample. The morphological, structural, compositional and textural characterization of the samples were obtained using scanning electron microscopy (SEM), transmission electron microscopy (TEM), X-ray powder diffraction (XRD), Raman spectroscopy, X-ray photoelectron spectroscopy (XPS), and N_2 physisorption respectively. The initial sample characterization confirmed bigger material agglomeration of the as-prepared mixed hydroxides compared to the NiCo-MnO_2 sample which had small stacked sheet-like and porous morphology. Further sample analysis also confirmed a high degree of crystallinity in both the mixed hydroxides and NiCo-MnO_2 samples with the elemental constituents existing in different oxidation states. One of the mixed hydroxides sample namely, $NiCo(OH)_2$ exhibited a specific surface area (SSA) of approximately 3.40 $m^2\ g^{-1}$ as compared to the ternary NiCo-MnO_2 material which exhibited a higher SSA of 153.94 $m^2\ g^{-1}$. The ternary NiCo-MnO_2 electrode exhibited the highest specific capacity of 132.1 mAh g^{-1}, compared to $NiCo(OH)_2$ and NiCoMn-triple hydroxide (NiCoMn-TH) electrodes which exhibited a specific capacities of 110.3 and 64.36 mAh g^{-1} respectively at a current density of 0.5 A g^{-1}. In addition, the ternary NiCo-MnO_2 electrode exhibited a better cycling stability compared to $NiCo(OH)_2$ electrode. Notably, an assembled NiCo-MnO_2//C-FP hybrid asymmetric supercapattery, displayed a specific capacitance of 130.67 F g^{-1}, high energy and

power densities of 48.83 Wh kg^{-1} and 896.88 W kg^{-1} at 1 A g^{-1} respectively. An excellent cycling stability with a coulombic efficiency of 99.98% and capacitance retention of 96.78 % was recorded for up to 10,000 cycles within an operating voltage of 1.5 V, at a 3 A g^{-1} current density

KEYWORDS: Mixed hydroxides; NiCo-MnO_2; Carbonized iron cations (C-FP); Electrochemical performance; Supercapattery; Energy density.

Graphical abstract

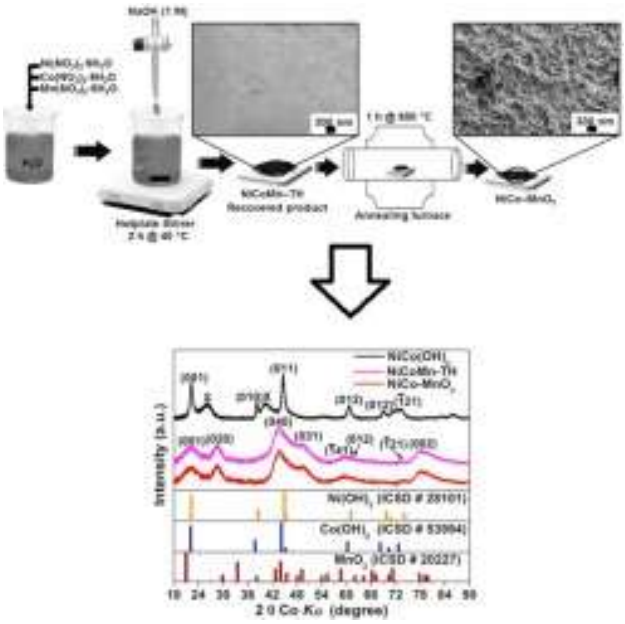

1. INTRODUCTION

High-performance energy storage devices are in great demand in modern society due to the development of numerous portable electronic devices and the emergence of hybrid electric vehicles. However, most of these new inventions require high-performance energy storage units with both high energy and power densities [1–4]. Among common electrical energy storage devices in use are lead–acid batteries, nickel–metal hydride batteries, lithium ion batteries (LIBs) and supercapacitors. Batteries with high energy density and supercapacitors (SCs) with excellent power density are currently considered to meet the needs of increasing energy demand [5]. LIBs can store a large amount of energy as high as 150-200 Wh kg^{-1}, but are confined to their low power density (below 1000 W kg^{-1}) and poor cycle life (usually less than 1000 cycles) [6,7].

Supercapacitors also known as electrochemical capacitors are a class of energy storage devices with the capability of giving off high power with capability of delivering energy in short period of time unlike batteries. Their low cost, low maintenance, relative safety and long cycle life makes them even more desirable for high-power delivery applications. Supercapacitors are used mainly as the power source in electric/hybrid electric vehicles, backup memories, airplane emergency doors, micro-devices and portable electronics [8]. Nevertheless, they are disadvantageous from the perspective of their poor energy density when compared to lithium ion batteries [9,10].

An assessment of various research studies related to energy storage device technology has shown an extensive efforts by many experts in the field to produce materials with desirable properties [11]. This led to the emergence of various syntheses techniques of new materials, most of which require high temperature reaction environments and a continuous power supply to obtain the final products. Presently, materials for energy storage devices with controlled morphology and properties are prepared using simple and low-temperature stirring technique [12–14]. The preparation technique is relatively simple, cost effective and relatively environmentally benign.

Generally, transition metal hydroxides are plagued with a low electrical conductivity but high specific capacitance due to their characteristic redox reaction. As such, they do not yield a high performance under high-rate current densities [15,16]. On the other hand, transition metal hydroxides/oxides have been intensely studied with a view to overcome the above limitation and refine their properties to fit the desired use [17–19]. Transition metal hydroxides/oxides are semi-conductive materials among which Ni based oxides have been taken into account as a promising candidate as electrode materials for electrochemical capacitors owing to its cost effectiveness, natural abundance as well as adequate electrochemical performance [16,20]. The latest progress of NiCo-based application for supercapacitor and battery have been reported in the literature [21–23]. Nevertheless, the demonstrated electrochemical performances of the so

called supercapacitor electrodes are nonetheless not enough, particularly in terms of energy density.

In this work, we report the synthesis of mixed transition metal hydroxides $NiCo(OH)_2$, NiCoMn-triple hydroxide (NiCoMn-TH) and ternary metal oxide (NiCo-MnO_2) materials via a facile low temperature process and the characterization/electrochemical testing as potential *SC* electrode materials with a view to highlighting some unique features which make them useful in this regard. The electrode materials were synthesized by force-driven hydrolysis of hydrated nitrate salts of nickel, cobalt and manganese salt at 40 °C for 2 h. The electrochemical performance of the electrode materials were analyzed in a three-electrode cell configuration using 1 M KOH electrolyte. The ternary NiCo-MnO_2 electrode exhibited the highest specific capacity of 132.1 mAh g^{-1}, compared to $NiCo(OH)_2$ and NiCoMn-TH electrodes which exhibited a specific capacities of 110.3 and 64.36 mAh g^{-1} respectively at a current density of 0.5 A g^{-1}. The complete asymmetrical cell displayed a specific capacitance of 130.67 F g^{-1}, high energy and power densities of 48.83 Wh kg^{-1} and 896.88 W kg^{-1} at 1 A g^{-1} respectively. An excellent cycling stability with a coulombic efficiency of 99.98% was recorded for up to 10,000 cycles at a current density of 3 A g^{-1}.

2. EXPERIMENTAL DETAILS

2.1. Preparation of materials

2.1.1. Preparation of $NiCo(OH)_2$

All the reagents used in this work were of analytical grade and used as received without further purification. The $NiCo(OH)_2$ sample was synthesised via a chemical precipitation process. Briefly, 1g of $Ni(NO_3)_2{\cdot}6H_2O$ together with 1g of $Co(NO_3)_2{\cdot}6H_2O$ were dissolved in 100 ml of deionised water. The solution was then stirred for 30 min to obtain a homogeneous mixture. Thereafter, 14 ml of 1M NaOH aqueous solution was added dropwise to maintain a pH of 10 for polarization, which changed the colour of the homogeneous mixture kept at 40 °C from brown to

bluish dark while magnetically stirring for 2 h. The resulting greenish dark precipitate was collected by centrifugation, washed several times with deionised water and ethanol, with the recovered solid particle put in an oven to dry at 60 °C overnight.

The following equation (1) below summarizes the reaction route to obtain $NiCo(OH)_2$.

$$\boldsymbol{Ni(NO_3)_{2_{(s)}} + Co(NO_3)_{2_{(s)}} + 2N_aOH_{(aq)} + H_2O_{(l)} \rightarrow NiCo(OH)_{2_{(s)}} + 2Na(NO_3)_{2_{(aq)}} + H_2O_{(l)}} \quad \textbf{(1)}$$

2.1.2. Preparation of NiCoMn-triple hydroxide (NiCoMn-TH) and ternary NiCo-MnO_2 composites

Using the same procedure as in 2.1.1., 0.67 g of $Mn(NO_3)_2{\cdot}4H_2O$, $Ni(NO_3)_2{\cdot}6H_2O$ and $Co(NO_3)_2{\cdot}6H_2O$ precursor salts were completely dissolved in 100 ml of deionized water whilst magnetically stirring the mixture. Subsequently, 14 ml of 1 M NaOH was added dropwise the homogeneous mixture kept at 40 °C for 2 h upon magnetic stirring. The resulting greyish-cream mixture was left to stand for about 10 h for complete precipitation. It was then centrifuged and washed several times with deionised water and ethanol. The solid precipitate was collected and dried in an oven at 60 °C for 12 h. The interim solid ternary nickel cobalt manganese triple

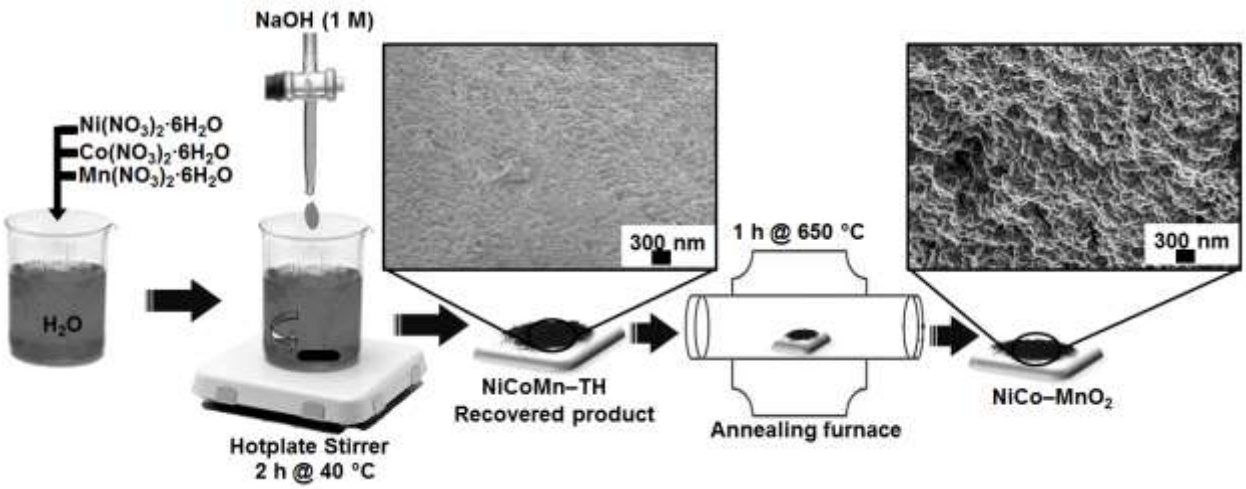

Scheme 1: Schematic of the synthesis process of NiCo-MnO_2 composite.

hydroxide (NiCoMn-TH) material was then annealed in air at 650 °C for 1 h at a ramping rate of 2 °C/min to obtain a more stable ternary NiCo-MnO_2 composite as shown in scheme 1 above:

2.1.3. Preparation of C-FP negative electrode material

Pyrolysis of the iron-containing mixture, denoted as C-FP was achieved by complete dissolution of iron (III) nitrate nonahydrate salt in ethanol, and mixed with PANI. The resulting mixture was sonicated for several hours to have slurry which was then coated onto nickel foam. The coated nickel foam was then transferred into a Quartz tube under N_2 atmosphere at 850 °C to enhance the adsorption of iron cations (Fe^{3+}) onto the PANI film (C-FP) which was deposited on a nickel foam template (*see Supplementary information for more details*).

2.2. Characterization of the samples

Scanning electron microscope (SEM) micrographs, energy dispersive X-ray (EDX) spectra and the transmission electron microscopy (TEM) micrographs of the as-prepared samples were obtained on a Zeiss Ultra Plus 55 field emission scanning electron microscope (FE-SEM) operated at 1.0 KV and a JEOL-2100F high-resolution transmission electron microscope (HRTEM FEI Tecnai-F30) alongside 200 KV acceleration voltage respectively. The structural analysis (X-ray diffraction (XRD)) was carried out using an XPERT-PRO diffractometer (PANalytical BV, Netherlands) with reflection geometry at 2θ values (18–90°) with a step size of 0.01°, operating with a Co *K*α radiation source (λ = 0.178901 nm) at 50 kV and 30 mA. A T64000 micro-Raman spectrometer (HORIBA Scientific, Jobin Yvon Technology) with a 514 nm laser wavelength and spectral acquisition time of 120 s was used to characterize the as-prepared samples. The Raman system laser power was set as low as 5 mW in order to minimize heating effects. Fourier transform-infrared (FT-IR) spectra of the samples were obtained using a Varian FT-IR Spectroscopy in the wavenumber range of 400 - 4000 cm^{-1}. X-ray photoelectron spectroscopy (XPS) measurements of the samples were conducted using a Physical Electronics VersaProbe 5000 spectrometer operating with a 100 μm monochromatic Al-Kα exciting source. N_2-absorption/desorption isotherms were obtained on a Micromeritics TriStar II 3020 system

operated in a relative pressure (P/P_o) range of 0.01–1.0 with pre-degassing of the samples at 100 °C for 18 h under vacuum prior to the measurement. The Brunauer-Emmett-Teller (BET) and Barrett–Joyner–Halenda (BJH) models were used to determine the surface area and the pore size distribution (PSD) of the samples respectively. XRF measurement of the pressed powder composite sample was performed using the ARL Perform'X Sequential XRF instrument with Uniquant software for analysis.

2.3. Electrochemical measurements

The electrodes were prepared by mixing the active material (80 wt%) with conductive acetylene carbon black (10 wt%) as a conducting agent and a PVDF binder (10 wt%), with a small amount of N-methyl-2-pyrrolidone (NMP) solvent added to the mixture with low-speed stirring to form a uniform slurry. The slurry was then coated onto nickel foam and dried at a temperature of 60 °C for 10 h. The capacitive performance of nickel foam-supported electrodes was investigated using a Bio-Logic VMP300 potentiostat (Knoxville TN 37,930, USA) controlled by the EC-Lab® V1.40 software in a three-electrode configuration. The electrochemical measurements were performed with a glassy carbon counter electrode, Ag/AgCl reference electrode, and the as-prepared mixed hydroxide materials as the working electrodes. All the electrochemical measurements for this study were performed in a 1 M KOH electrolyte at room temperature. The mass loading of the active material was estimated to be ca. 2.5 mg, 2.34 and 2.3 mg for the $NiCo(OH)_2$, NiCoMn-TH and NiCo-MnO_2 electrodes respectively. The cyclic voltammetry (CV) of the as-prepared samples were carried out at different scan rates from 1 to 50 mV s^{-1} within a potential window range of -0.1 to 0.4 V vs. Ag/AgCl. The galvanostatic charge-discharge (GCD) measurement was carried out at different current densities in the range of 0.5 to 5.0 A g^{-1} in a potential window range of -0.1 V to 0.4 V. The electrochemical impedance spectroscopy (EIS) of the samples was conducted in an open-circuit potential and in a frequency range of 10 mHz to 100 kHz.

The gravimetric specific capacitance, C_s (Fg^{-1}) of the half-cell was derived from the CV curves according to the formula stated in equation 2 below [24]:

$$C_s = \frac{1}{mS_c\Delta V}\int_{v_1}^{v_2} IdV \quad (2)$$

where, v_1 and v_2 are the vertex potential of the potential range, I is the current response (mA), ΔV is the cell voltage (V) for the single electrode, S_c is the scan rate (mVs^{-1}) and m is the loading mass (g) of the single electrode.

The specific capacity, Q_s (mAh g^{-1}), energy efficiency of the materials using GCD curves were calculated according to the following relations [8, 9][11]:

$$Q_s = \frac{It}{3.6m} \quad (3)$$

$$\eta_E = \frac{E_d}{E_c} \times 100 \quad (4)$$

where *I* is the discharge current in mA, *m* is the mass loading of the electrode in mg, and *t* is the time in seconds taken for a complete discharge cycle. η_E, E_d and E_c are energy efficiency, discharge energy and charge energy from the integral of the area under the charge-discharge curve of the electrode respectively.

The specific capacitance, C_s, energy and power densities of the full hybrid asymmetric supercapattery (composed of the ternary NiCo-MnO_2 and C-FP selected as both positive and negative electrode respectively), with respect to the current density of the device were evaluated from the slope of the discharge curve according to following equations:

$$C_s = \frac{I \times \Delta t}{m \times \Delta V} \quad [F\ g^{-1}] \quad (5)$$

$$E_d = I/3.6m \int V dt \quad [Wh\ kg^{-1}] \quad (6)$$

$$P_d = 3.6 \times E_d/\Delta t \quad [kW\ kg^{-1}] \quad (7)$$

where .C_s is the specific capacitance of the electrode based on the mass of the active material, I is the discharge current in Amperes (A), m is the mass loading of the active material in grams (g). ΔV is the operating potential window in volts (V), Δt in seconds is the electrode discharge time respectively, E_d & P_d, are the energy and power densities respectively with their specified units.

The maximum constant-current discharge power density, P_{max} of the hybrid cell was predicted using the effective solution resistance, R_s (ohm) determined from the Z'-intercept of the Nyquist plots of frequency analysis according to the following equation [27,28]

$$P_{max} = \frac{V^2}{4mR_s} \quad (8)$$

Where V (V) and m (g) are the potential window as well as the mass loading of the active material respectively.

The fabricated hybrid asymmetry SC could operate in a wider potential window, *ca.* 1.50 V. For optimal performance of the hybrid asymmetry device, the mass on each electrode was balanced using the charge balance equation, $Q_+ = Q_-$,with the charge stored on each electrode expressed as [29]:

$$Q = C_s \times m\,\Delta V \quad (9)$$

where Q (C) is the stored charge on the electrode, C_S (F g^{-1}) is the specific capacitance of the electrode based on the mass of active material, m (g) is the mass of active material, and ΔV (V) is the potential window.

The mass balancing between the positive and negative electrodes was accurately determined by further considering [30]:

$$\frac{m_+}{m_-} = \frac{C_{s-}\ \Delta V_-}{C_{s+}\ \Delta V_+} \quad (10)$$

3. RESULTS AND DISCUSSION

3.1. Morphological, structural and composition characterization

Fig. 1 shows the SEM and TEM morphologies of the as-prepared materials. Fig. 1 (a) and (b) represent low and high magnifications SEM images of $NiCo(OH)_2$. It can be seen that the as-prepared $NiCo(OH)_2$ has an agglomerated larger flake-like morphology compared to the NiCo-MnO_2 sample which shows a singly stacked porous sheet-like as shown in Fig. 1 (c and d). The morphology of the samples was further analyzed by TEM technique as shown in Fig. 1 (e and f). The TEM micrographs clearly show the agglomerated flake-like particles of $NiCo(OH)_2$ (Fig. 1 (e)) and the singly stacked porous sheet-like structures of the NiCo-MnO_2 (Fig. 1 (f)) in accordance with SEM results.

Fig. S1 in the supporting information displays the SEM micrographs of the NiCoMn-TH electrode material at low and high magnifications and the TEM micrograph to further observe the material morphology. It can be seen from the microscopy images that NiCoMn-TH material is composed of stacked flake-like nano structures which is further confirmed by the TEM image as shown in Fig. S1 (c). Visible flakes are clearly seen in the TEM micrograph overlapping each other in different orientations.

Fig. S2 shows the SEM and TEM micrographs of the as-synthesized C-FP negative electrode material of the hybrid NiCo-MnO_2//C-FP supercapattery. It can be observed that the material mainly composed of orthorhombic nano grains at low and high magnifications respectively. These microstructures were further confirmed by TEM as shown in Fig. S2 (c-d). The TEM micrographs clearly show the nano sized particles of the material.

The purity and phase structure of the as-prepared materials were observed using X-ray diffraction (XRD). Fig. 2 (a) shows the powder XRD spectrum of the samples with the matching inorganic crystal structure database (ICSD) card no. 28101 for $Ni(OH)_2$ crystal system: (trigonal; space-group: *P*-3*m*1; cell parameters: a = 3.1300 Å, c = 4.6300, b = 3.1299 Å), ICSD card no. 88940 for $Co(OH)_2$ crystal system: (trigonal; space-group: *P*-3*m*1; cell parameters: a = 3.186 Å,

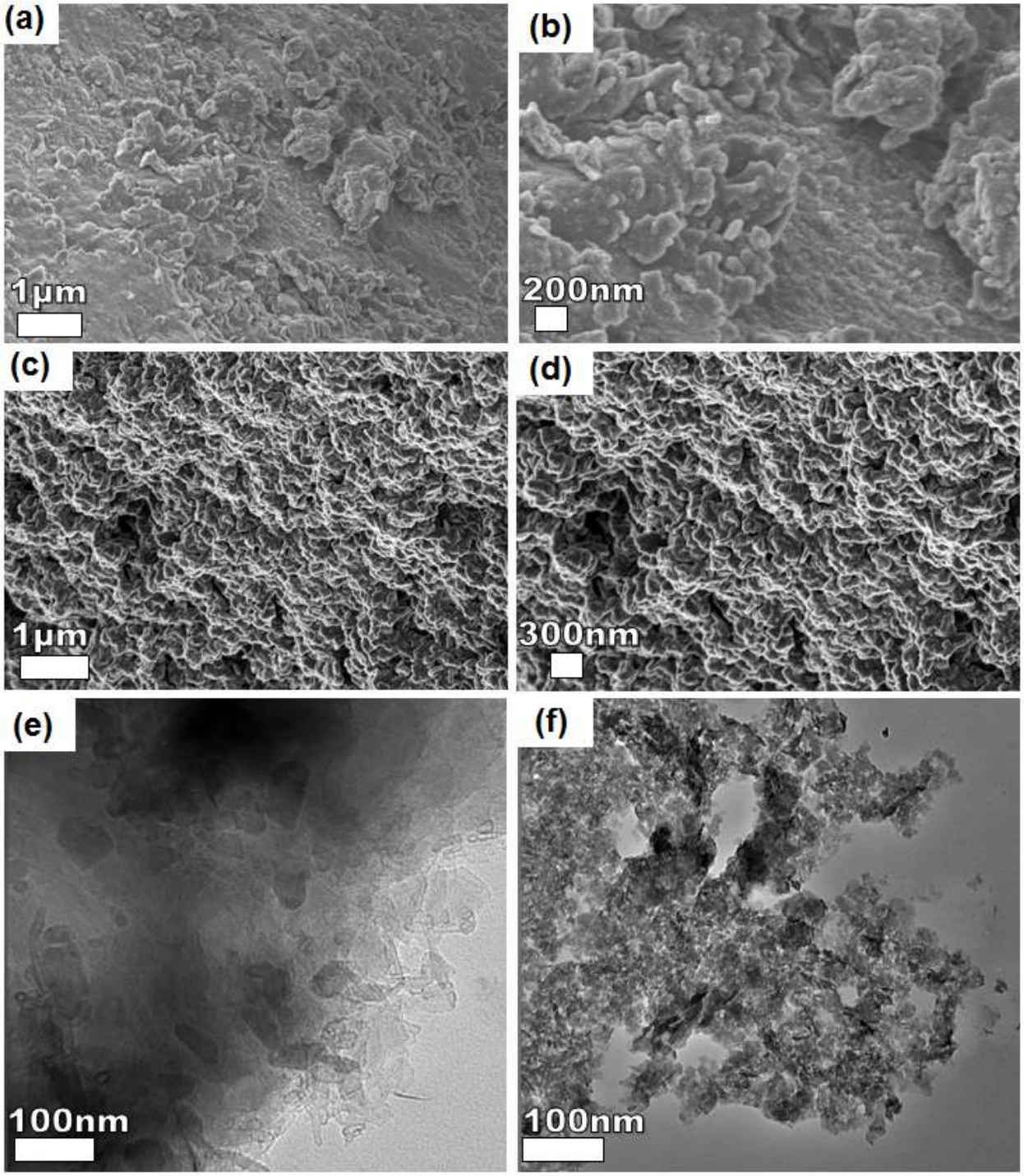

Fig. 1. (a, b) SEM images of the as-prepared $NiCo(OH)_2$ at low and high magnifications respectively. (c, d) SEM images of the as-prepared NiCo-MnO_2 at low and high magnifications respectively. (e, f) TEM images of the $NiCo(OH)_2$ and NiCo-MnO_2 respectively.

c = 4.653 Å, *b* = 3.1859 Å), and ICSD card no. 20227 for MnO_2 crystal system: (tetragonal; space-group: *I*4/*m*; cell parameters: *a* = 9.8151 Å, *c* = 2.8471 Å, *b* = 9.8154 Å). The XRD spectrum of $NiCo(OH)_2$ sample shows the typical diffraction of the transition metal hydroxide

phases and matches well with the patterns of the $Ni(OH)_2$, ICSD card no. 28101 and $Co(OH)_2$, ICSD card no. 88940 standards, except, for peaks indicated by X which could be possibly due to defects. Using equation ES2 (*see supplementary information*), the NiCo-MnO_2 electrode material has an average crystallite size of 8.62 nm compared to 15.45 nm observed for $NiCo(OH)_2$ material, suggesting that the NiCo-MnO_2 with smaller particle size is more nanocrystalline in nature, which accounts for the material's enhanced electrochemical results. Fig. 2(b) is a 2×2×2 cell of $Ni(OH)_2$, $Co(OH)_2$ and MnO_2 viewed along y-axis based on Crystallographic Information Files (CIF) of above-mentioned ICSD cards. The $Ni(OH)_2$ has an O–H distance of 1.06 Å, with Ni^{2+} ion-ion interaction taking place via the oxygen ions since the Ni–Ni distance (4.63 A) is much greater than the sum of ionic radii of Ni–Ni [31]. These indirect interactions, including interaction via Ni–OH–OH–Ni ions could be responsible for the magnetic nature often seen in $Ni(OH)_2$ as well as in $Co(OH)_2$ [31,32]. Also, Fig. 2 (a) shows the XRD spectrum of NiCo-MnO_2 with broader diffraction peaks matching well the MnO_2 (ICSD 20227) standard. The peak broadening can be attributed to the sample's reduced crystallites size, which agrees well with SEM and TEM results. This can be attributed to the high surface area-to-volume ratio of the material which would lead to an increase in the amount of interfaces and enhanced electron and mass transport yielding electrode with much higher electrochemical performance. The MnO_2 structure is composed of more oxygen atoms with most manganese atoms located in the center of the structure (Fig. 2 (b)). Hence, XRD results affirm further the synthesis of the materials.

A representative XRD spectrum and the matching ICSD card of the as-prepared C-FP material indexed using the matching Inorganic Crystal Structure Data-base (ICSD) card no. 16593 with chemical formula Fe_3C is displayed in S3 (a) of the Supplementary information, with well-defined diffraction peaks and identified crystal planes of Fe_3C phase respectively. The expected broad but weak diffraction peak around 30° corresponding to the (002) plane of graphitic carbon is observed, indicating presence of particular graphitic structures. A diffraction (320) peak

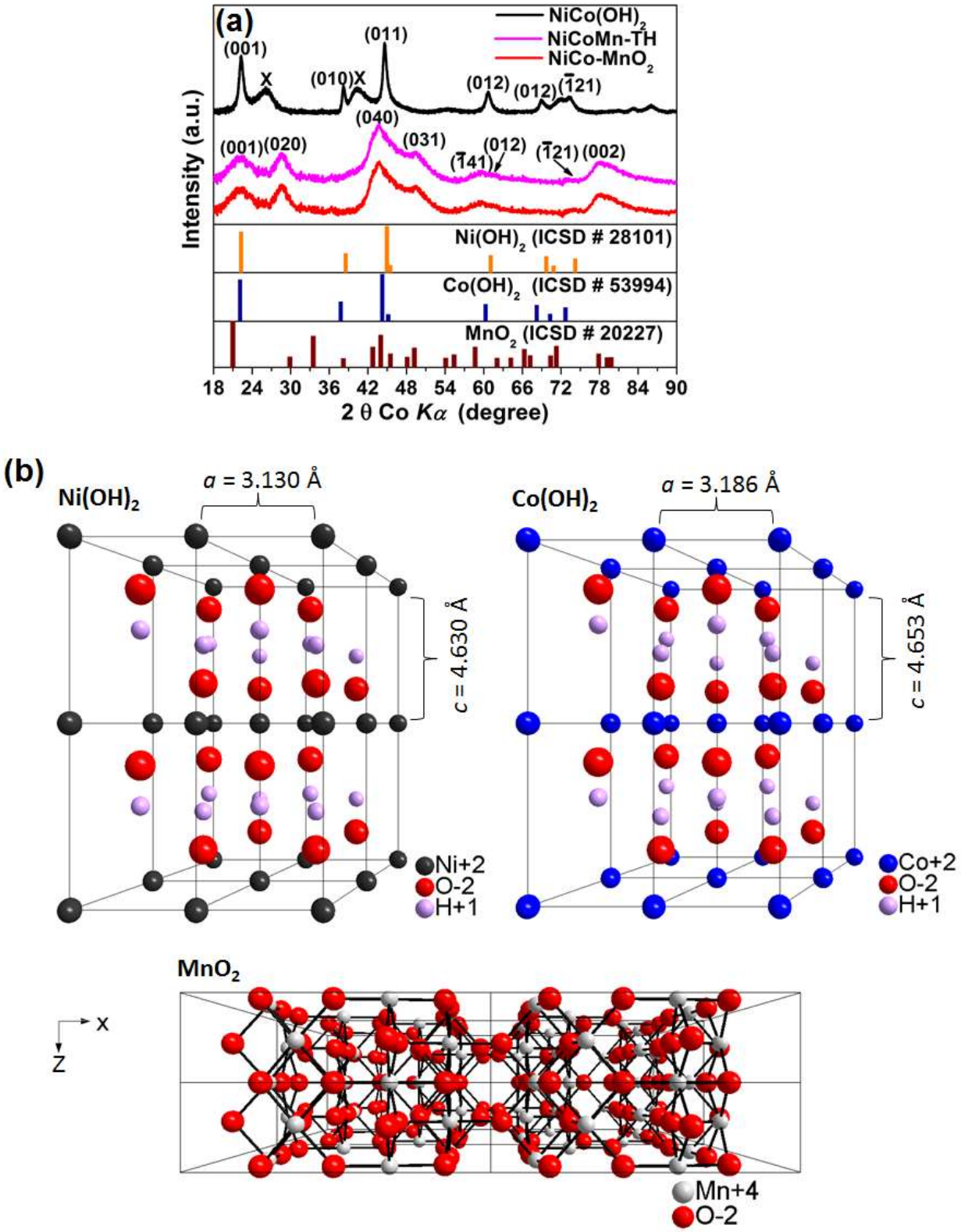

Fig. 2. (a) The X-ray diffraction of the as-prepared $NiCo(OH)_2$, NiCoMn-TH and $NiCo\text{-}MnO_2$ samples, and the matching ICSD cards for $Ni(OH)_2$, $Co(OH)_2$ and MnO_2. (b) 2×2×2 cells of $Ni(OH)_2$,$Co(OH)_2$ and MnO_2 viewed along y-axis.

around 52.5° is due to presence of metallic Fe and Ni. The two peaks at around 44.2° and 64.3° can be attributed to the (110) and (200) reflections of α-Fe, respectively (JCPDS, No. 870722). The other diffraction peaks present are characteristic of the crystalline planes of Fe_3C species (JCPDS, No. 892867). A further description of the nature of the peaks is discussed in the supplementary information.

It is observed that the NiCoMn-TH and NiCo-MnO_2 exhibited similar crystal structure as shown in Fig. 2 (a). However, further sample characterization were focused on the $NiCo(OH)_2$ and $NiCoMnO_2$ due to the poor electrochemical performance recorded for the NiCoMn-TH sample since the main focus area of this present study is related to the electrochemical performance. This will be discussed at a later stage in Fig. 8 where the three electrode materials are compared.

Fig. 3(a) shows the Raman spectra of the as-prepared $NiCo(OH)_2$ and NiCo-MnO_2 samples which were fitted to a combination of Lorentzian and Gaussian modes. In Fig. 3 (a), the Raman spectrum of the as-prepared $NiCo(OH)_2$ sample shows modes at 310, 458, 558 and 649 cm^{-1}. These modes were compared to those reported in earlier studies [33,34] for $Ni(OH)_2$ and $Co(OH)_2$. It is worth mentioning that a group theory analysis of the phonon modes in brucite-type hydroxides (e.g., $Ni(OH)_2$ and $Co(OH)_2$) predicts that four Raman active modes are allowed, three of which are lattice modes in the range of 310-530 cm^{-1}, and one is a symmetric OH stretching vibration at about 3581 cm^{-1} [35,36]. In addition, $Co(OH)_2$ and cobalt oxyhydroxide, CoO(OH), show Raman active modes at 557 and 641 cm^{-1} respectively [37,38]. Therefore, the observed Raman modes of $NiCo(OH)_2$ sample reveals the major vibrational features of the $Ni(OH)_2$, $Co(OH)_2$ and CoO(OH). The NiCo-MnO_2 sample also displayed Raman active modes at 502, 584 and 625 cm^{-1} wavenumber, as shown in Fig. 3(a). These modes agree well with the three major vibrational features of the MnO_2 previously reported at 500, 585, and 625 cm^{-1} on similar materials [39,40]. Thus, this confirms MnO_2 compound in the sample and the

relatively high intensity of these modes suggest that a relatively high MnO_2 content is present in the NiCo-MnO_2 sample.

Fig. 3 (b) shows the FT-IR spectra of the as-prepared materials. As depicted in Fig. 3 (b), the band at about 3480 cm^{-1} is assigned to O–H stretching vibrations and that at 1600 cm^{-1} is assigned to O–H bending vibrations, and both bands can be predominantly due to the

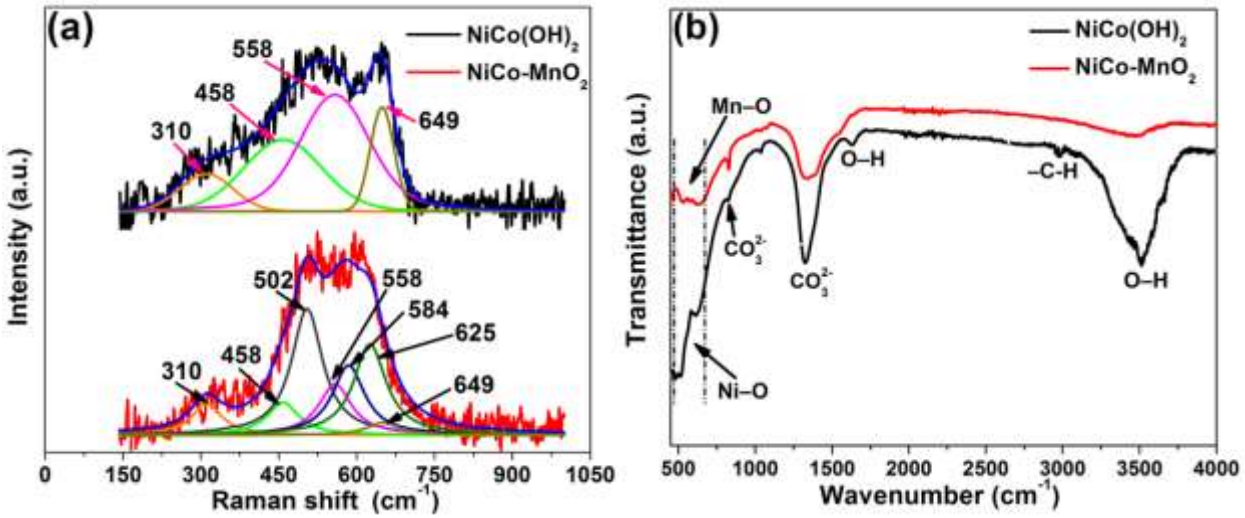

Fig. 3. (a) The Raman spectra and (b) The FT-IR spectra of the as-prepared $NiCo(OH)_2$ and NiCo-MnO_2. Raman spectra were fitted to a combination of Lorentzian and Gaussian modes.

complexation of metal-hydroxyl groups [41–43]. In fact, the IR band at ~1600 cm^{-1} is usually ascribed to H_2O bending vibration features. The band at 2980 cm^{-1} is ascribed to the –C–H vibration mode of $–CH_2$ [42]. The IR band at 1350 cm^{-1} is assigned to CO_3^{2-} asymmetrical stretching vibrations, while a band at 830 cm^{-1} is assigned to the bending vibrations of CO_3^{2-} [41–43]. The bands in the range of 500-640 cm^{-1} can be assigned to the M–O, O–M–O, and M–O–M (M= Co, Ni and Mn) lattice vibrations [43,44]. In comparison between $NiCo(OH)_2$ and $NiCoMnO_2$, it can be seen that the broadband at 3480 cm^{-1} belonging to the O–H vibrations disappears confirming the transformation of $NiCo(OH)_2$ to NiCo-MnO_2.

Fig. 4 (a) and 4 (b) show the EDX spectra of the as-prepared $NiCo(OH)_2$ and NiCo-MnO_2 respectively. In the figures, it is seen that both the $NiCo(OH)_2$ and NiCo-MnO_2 materials are composed of Ni, Co and O with an additional Mn peak in the NiCo-MnO_2 spectrum. Both samples reveal traces of chlorine (Cl) which could be linked to the sample preparation, while the high C content arose from the carbon coating step adopted for measurements carried out by EDX-SEM system.

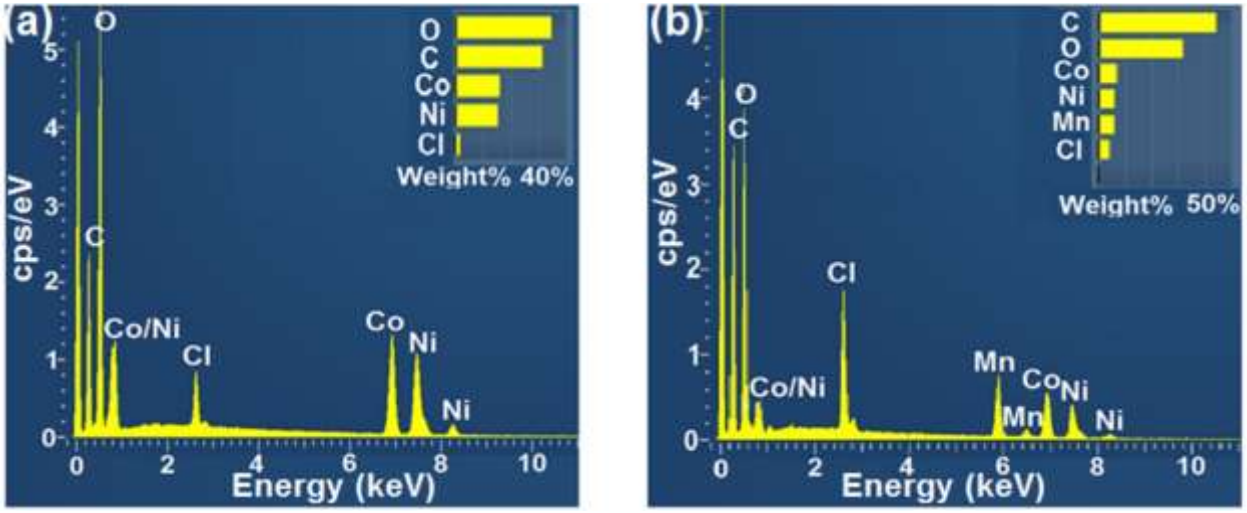

Fig. 4. EDX spectra of the as-prepared (a) $NiCo(OH)_2$ and (b) NiCo-MnO_2 samples.

The elemental and structural clarification analysis of the C-FP negative electrode material are shown in Fig. S3 (b). The analysis shows iron (Fe) and carbon (C) as the major elements with high content. The Sulphur (S) and Nitrogen (N) are linked to the PANI composition. A detailed description of the percentage weight of these elements is described in the supplementary information.

In addition to the bulk elemental composition of the samples, the surface elemental composition of the as-prepared $NiCo(OH)_2$ and NiCo-MnO_2 samples was analyzed by XPS. Fig. 5 (a) shows the wide scan XPS spectra of the as-synthesized $NiCo(OH)_2$ which displays the main elements (Ni, Co, and O) of the composition of the sample with fractional concentrations of 17.65 at% Ni 2p, 20.90 at% Co 2p and 52.61at% O 1s. The sample shows traces of 6.24 at% C 1s and 2.60 at% Cl 2s which could be due to sample preparation and handling through air.

Fig. 5 (b) shows the core level spectrum of Co 2p of the $NiCo(OH)_2$ sample which reveals the binding energy peaks at 780.4 eV and 785.5 eV which were fitted to Co $2p_{3/2}$, and other binding energy peaks at 795.9 eV and 802.5 eV which correspond to Co $2p_{1/2}$ core level. The fitted Co $2p_{3/2}$ peaks suggests that the Co oxidation state of the as-synthesized $NiCo(OH)_2$ is predominantly Co(II) (2+ valence state) with a fitted peak at 780.1 eV corresponding to CoO

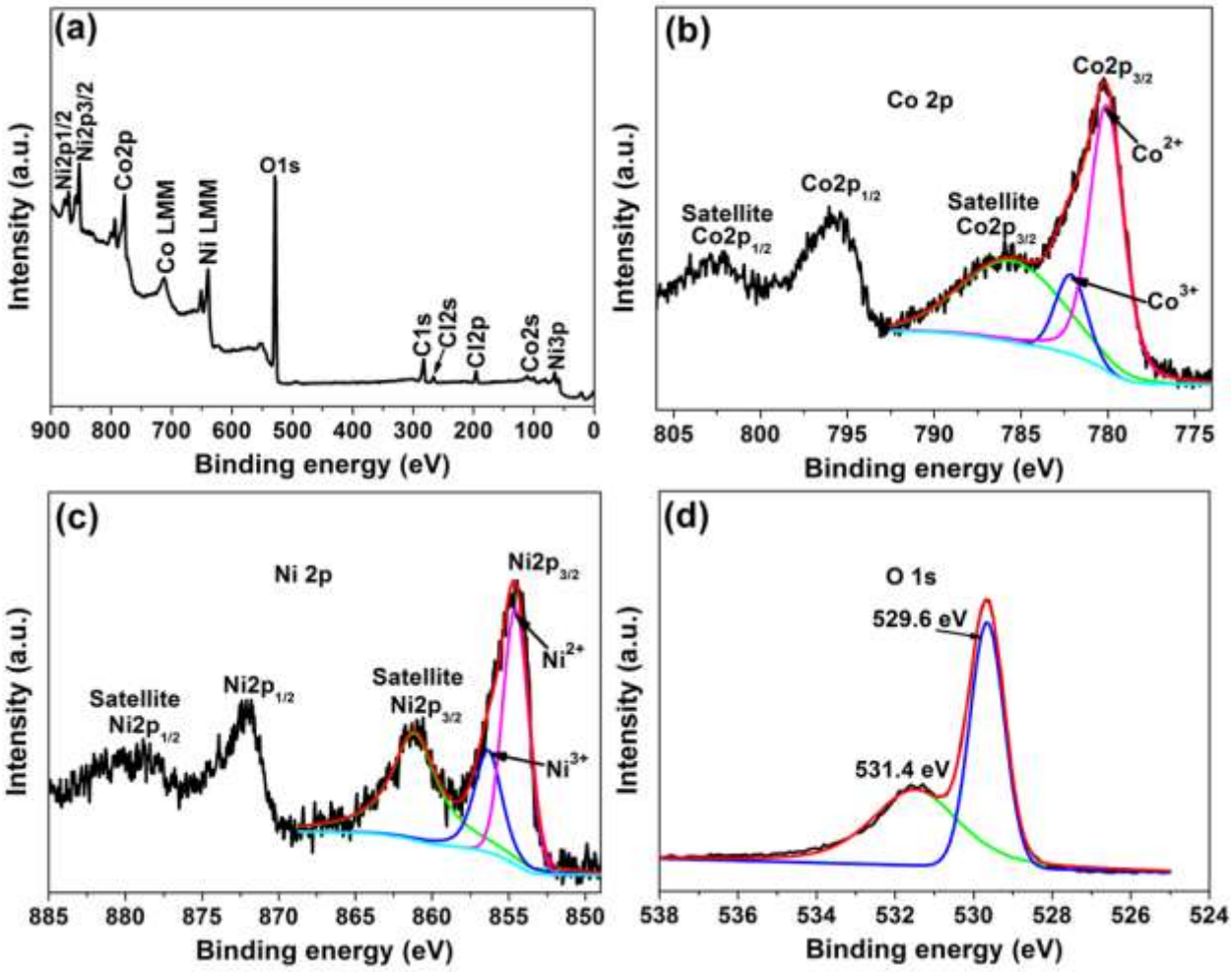

Fig. 5. (a) The wide scan XPS spectra of the as-received $NiCo(OH)_2$ sample. The core level spectrum of (b) Co 2p, (c) Ni 2p and (d) O 1s of a $NiCo(OH)_2$ sample.

$2p_{3/2}$ core level with a binding energy of 780.2 eV. The core level spectrum of Ni 2p of a $NiCo(OH)_2$ sample reveals the binding energy peaks at 854.4, 861.0 corresponding to Ni $2p_{3/2}$ core level, and 872.1 and 879.3 eV which correspond to Ni $2p_{1/2}$ core level. Similar to the fitted Co $2p_{3/2}$ peaks, the fitted Ni $2p_{3/2}$ peaks suggests that the Ni oxidation state of the sample is

predominantly Ni^{2+} [45–47]. Additionally, a binding energy peak at about 854.1 eV suggests the presence of CoNi bond since the CoNi $2p_{3/2}$ core level has a binding energy peak at 853.09 eV.

Furthermore, Fig. 5 (d) shows the core level spectrum of O 1s with fitted peaks at 529.6 and 531.4 eV which could be ascribed to O 1s in Ni–O and Co–O compounds. The XPS of the as-synthesized $NiCo(OH)_2$ reveals two mixed oxidation states. The two states, Ni^{2+}/ Ni^{3+} and Co^{2+} /Co^{3+} are mixed in the materials since there is no obvious difference in the diffraction patterns of the hydroxides (Fig. 2). Both Ni^{2+}/Ni^{3+} and Co^{2+}/Co^{3+} redox couples ensure a major electrocatalytic effectiveness [48] based on the synergistic redox reaction involving the changes in oxidation states with OH^- present in KOH electrolyte.

The wide scan XPS spectra of the annealed NiCo-MnO_2 (as shown in Fig. 6 (a)), displays the main elements (Ni, Co, Mn and O) of the composition of the sample with fractional concentrations of 10.10 at% Ni 2p, 13.30 at% Co 2p, 21.15 at% Mn 2p and 50.60 at% O 1s. This sample also shows traces of 3.24 at% C 1s, 1.30 at% Cl 2s and 0.31 at% N 1s. The core level spectrum of Mn 2p of the NiCo-MnO_2 sample reveals the binding energy peaks at 639.4 and 651.0 eV which agree with Mn $2p_{3/2}$ and Mn $2p_{1/2}$ core levels, respectively, shown in Fig. 6 (b). The fitted Mn $2p_{3/2}$ peaks suggests that the Mn oxidation state of the sample is composed of both Mn^{3+} and Mn^{4+} [49].

Similar to the core level spectra of Co 2p and Ni 2p of a $NiCo(OH)_2$ sample, the core level spectra of Co 2p and Ni 2p of the NiCo-MnO_2 sample reveal the oxidation states of Co and Ni (see Fig. 6 (c) and 6 (d)). However, the observed peaks are slightly shifted suggesting a change in the binding energy of a core electron of these elements predominantly due to a change in the chemical bonding of these elements (i.e., chemical change from $NiCo(OH)_2$ to NiCo-MnO_2). Fig. 6(e) shows the core level spectrum of O 1s with fitted peaks at 526.9, 528.4 and 529.7 eV which could be ascribed to O 1s in Ni–O, Co–O and Mn–O compounds.

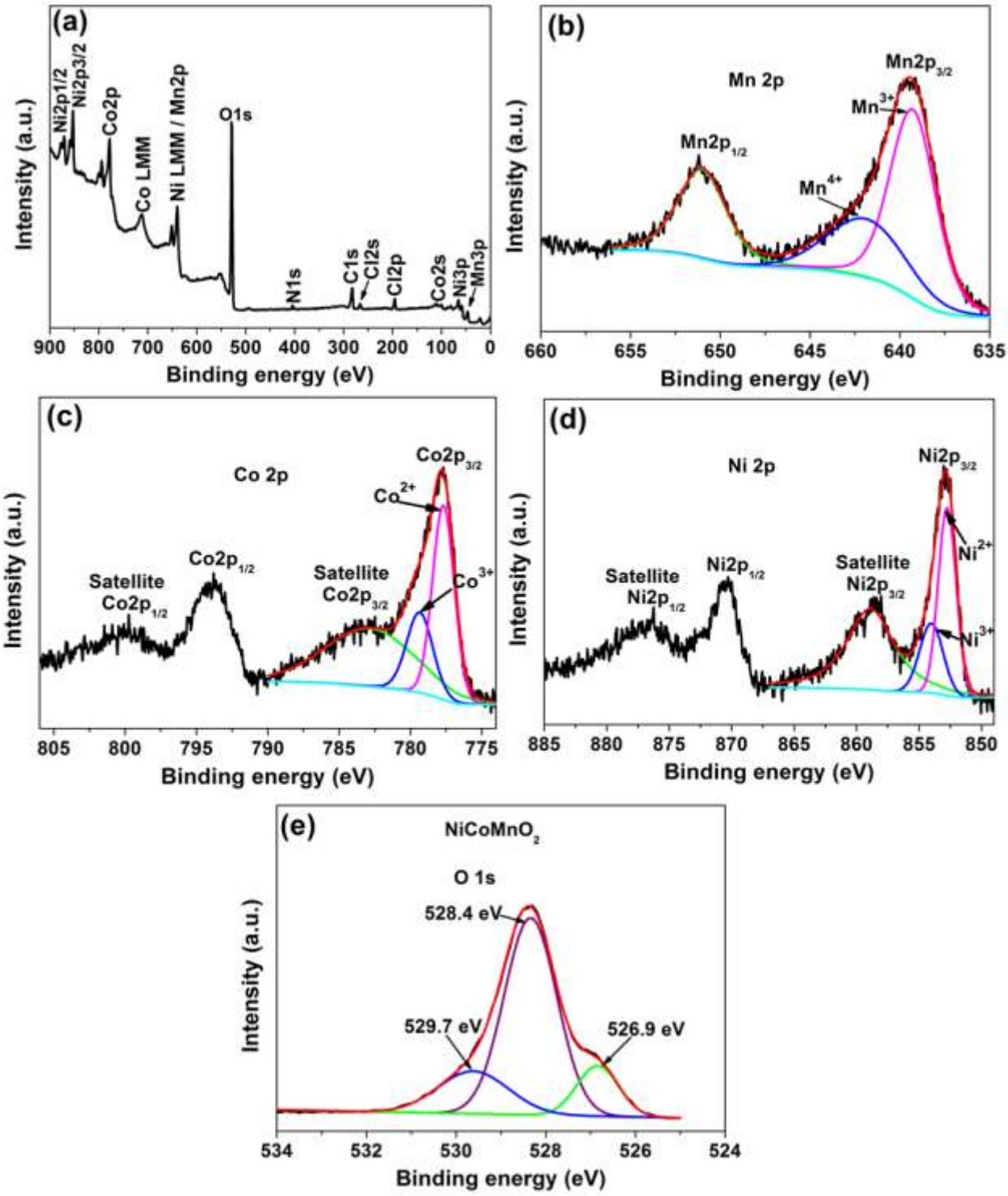

Fig. 6. (a) The wide scan XPS spectra of the as-received NiCo-MnO_2 sample. The core level spectrum of (b) Mn 2p, (c) Co 2p, (d) Ni 2p and (e) O 1s of a NiCo-MnO_2 sample.

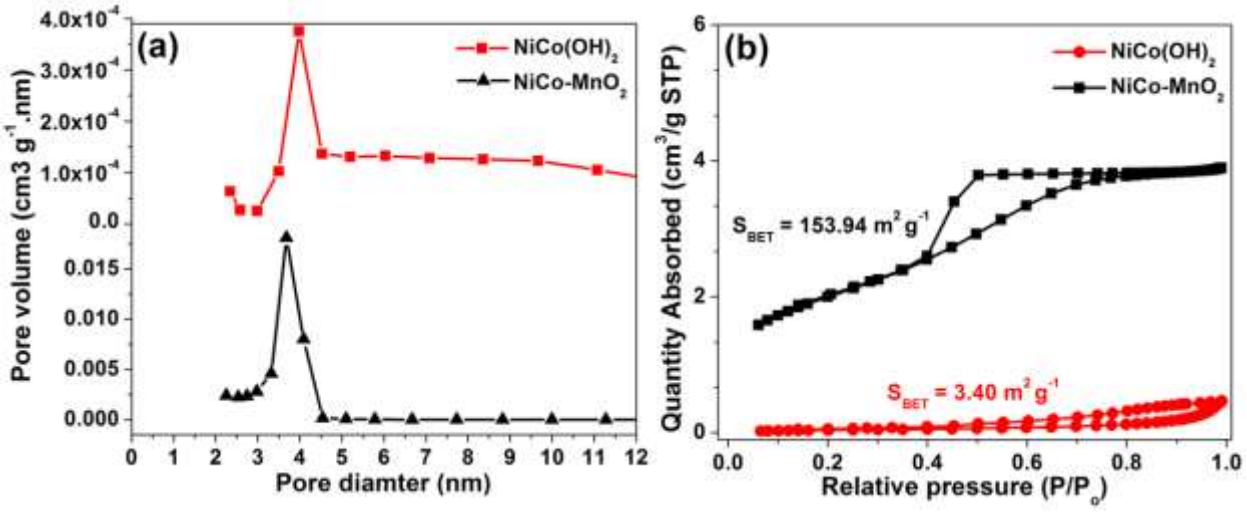

Fig. 7. (a) Pore size distribution and (b) N_2 isotherms of $NiCo(OH)_2$ and $NiCo\text{-}MnO_2$ samples.

Fig. 7 (a) shows the pore-size distribution curves of the as-prepared material, showing the presence of a mesoporous structure within the as-prepared material. The higher pore volume recorded is an order of magnitude higher for the $NiCo\text{-}MnO_2$ sample as compared to the $NiCo(OH)_2$ sample. The PSD results also confirms the observed enhancement in the SSA

recorded with the $NiCoMnO_2$ sample exhibiting a high BET specific surface area of 153.94 m^2g^{-1} compared to the $NiCo(OH)_2$ which exhibited 3.40 m^2g^{-1} as shown from the absorption-desorption isotherm in Fig. 7 (b). The textural properties could also be linked to the morphological characterization (TEM) results earlier discussed where an agglomerated flake-like sample morphology was seen for the $NiCo(OH)_2$ material as compared to the porous non-agglomerated stacked sheet-like particles morphology for the $NiCo\text{-}MnO_2$ sample.

The molar ratio of Ni: Co: Mn in the ternary metal oxide was given by the XRF measurement as 0.85:1:0.89 respectively as shown in Table S2 in the supplementary information. These measured Ni: Co: Mn ratios are in agreement with what was determined by the EDX analysis (Fig. 4 (b)). The ARL Perform'X Sequential XRF instrument with Uniquant software is used to analyze all elements in the periodic table between Na and U, but only elements found above the detection limits are reported.

3.2. Electrochemical characterization

3.2.1. Three-electrode electrochemical measurements of half-cell electrodes

To investigate the electrochemical performance of the as-prepared electrode materials, initial three-electrode measurements were carried out in 1 M KOH electrolyte. Fig. 8 (a) shows the charge-discharge (CD) curves of the $NiCo(OH)_2$, NiCoMn-TH and $NiCo\text{-}MnO_2$ at a current density of 0.5 A g^{-1} in a potential window range of -0.1–0.4 V. In comparison to the $NiCo(OH)_2$ and NiCoMn-TH electrodes, the $NiCo\text{-}MnO_2$ electrode exhibited a longer discharge time. Therefore, the CD curves clearly show that the addition of manganese to the nickel cobalt hydroxide with further annealing step significantly improves the capacity of the material. In addition, the nonlinear CD curves of the electrodes show potential steps, corresponding to a fast drop in the potential range of about 0.4–0.3 V and a slow drop in the potential range of about 0.3–0.2 V, suggesting faradic behavior of the electrode materials. Similarly, Fig. 8 (b) shows the associated CV curves of $NiCo(OH)_2$, NiCoMn-TH and $NiCo\text{-}MnO_2$ electrodes at a scan rate of 20 mV s^{-1} in a potential window range of -0.1–0.4 V which reveals that the $NiCo\text{-}MnO_2$ electrode has a high current response suggesting a high specific capacity. Thus, as hinted earlier, there was no further need to analyze the intermediate NiCoMn-TH but rather focus on the annealed $NiCo\text{-}MnO_2$ material electrode. Fig. 8 (c) shows the CV curves of $NiCo\text{-}MnO_2$ and nickel foam taken at a scan rate of 1 mV s^{-1} in the potential range of -0.1 - 0.4 V. It can be observed that the redox peaks of Ni-foam are negligible in comparison with that of as-synthesized ternary transition metal oxide. Nevertheless, it is believed that the redox peaks are substantively ascribed to electrode materials [50]. The two redox peaks can be ascribed to the electrochemical reactions of Ni-Co-Mn species according to the equations below:

$$NiO + OH^- = NiOOH + e^- \quad (11)$$

$$C_{o_3}O_4 + H_2O + OH^- = 3C_oOOH + e^- \quad (12)$$

$$M_nO + OH^- = M_nOOH + e^- \quad (13)$$

$$N_iC_oM_nO_4 + OH^- + H_2O = N_iOOH + C_oOOH + M_nOOH + e^- \quad (14)$$

$$M_nOOH + OH^- = M_nO_2 + H_2O + e^- \quad (15)$$

Besides, the peak current of the NiCo-MnO_2 is much higher than those of $NiCo(OH)_2$ and NiCoMn-TH at the same scan rate. Also, it has been proven that the area under the CV curve reflects the electrochemical performance of the electrode materials. The higher the response current density is, the larger the specific capacitance of the material is delivered [51]. We can infer that the NiCo-MnO_2 proved a better capacitance/capacity than those of $NiCo(OH)_2$ and NiCoMn-TH.

To further investigate the electrochemical performance of NiCo-MnO_2 electrode material, the CD curves were obtained at different current densities (Fig. 9 (a)), while the CV curves were obtained at different scan rates (Fig. 9 (b)), in a potential window range of -0.1–0.4 V. The nonlinear CD curves and the CV curves show oxidation and reduction peaks at approximately 0.1 V and 0.3 V corresponding to anodic and cathodic peaks respectively. This is as a result of the reversible redox faradaic reaction of a mixed composition, containing Ni^{2+},Ni^{3+}, Co^{2+}, Co^{3+}, Mn^{2+} and Mn^{3+} [52–54] confirming the faradic property of the NiCo-MnO_2 electrode material. According to equation 2, the NiCo-MnO_2 electrode has a maximum specific capacitance of 1205.1 Fg^{-1} compared to 991.85 and 231.69 Fg^{-1} for the $NiCo(OH)_2$ and NiCoMn-TH electrodes all at a scan rate of 5 mVs^{-1} respectively. Using equation 3, the specific capacities of the NiCo-MnO_2 electrode material were calculated and plotted as a function of current densities as shown in Fig. 9 (c).

For further comparison, the specific capacity of the $NiCo(OH)_2$ electrode is shown in Fig. 9 (c) which is smaller compared to that of the NiCo-MnO_2 electrode. In Fig. 9 (c), it can be seen that the specific capacity decreases with the increasing current density and this could be attributed to

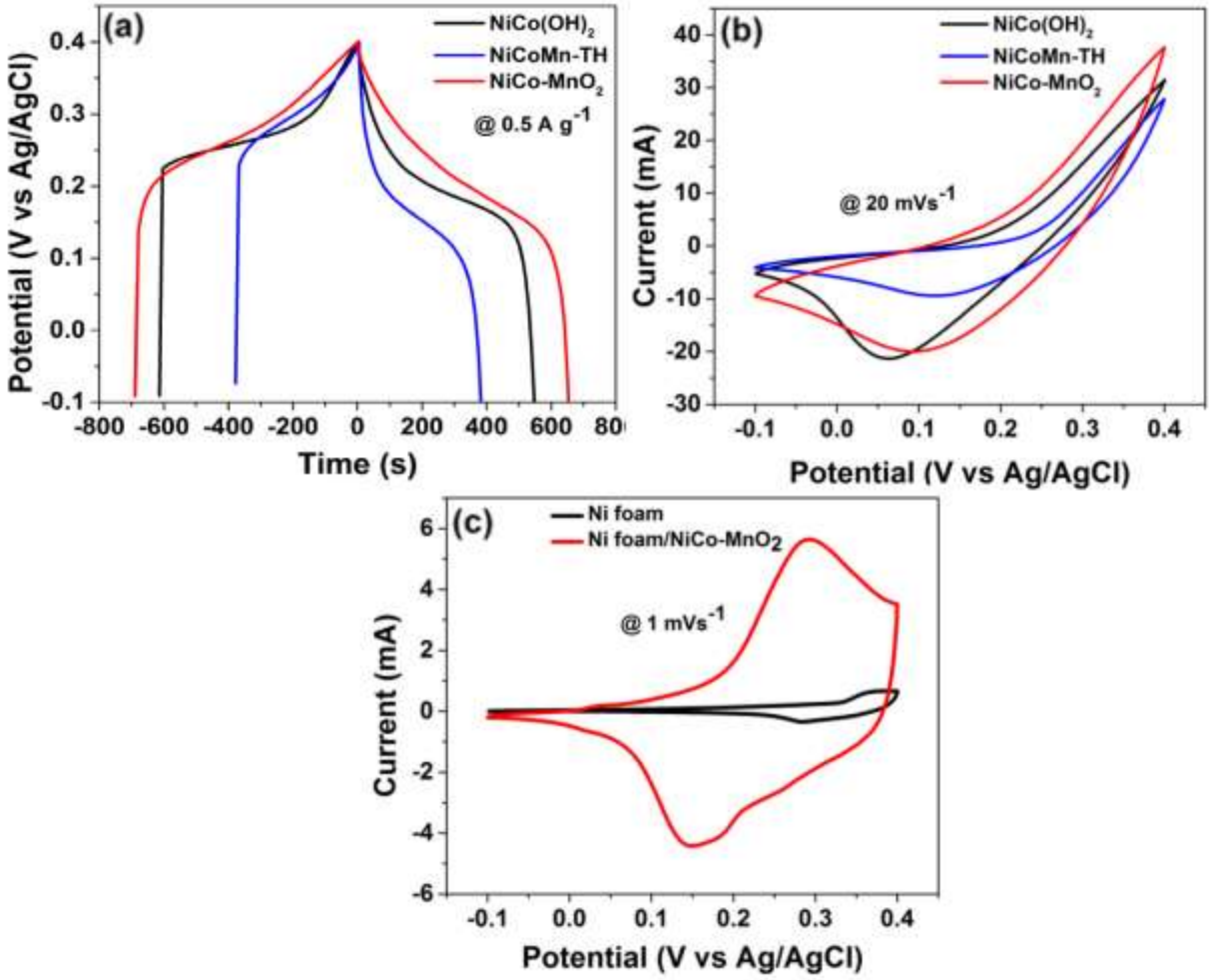

Fig. 8. (a) CD curves of $NiCo(OH)_2$, NiCoMn-TH and $NiCo\text{-}MnO_2$ at a current density of 0.5 A g^{-1}, (b) CV curves of $NiCo(OH)_2$, NiCoMn-TH and $NiCo\text{-}MnO_2$ at a scan rate of 20 mVs^{-1} and (c) CV curves of ternary metal oxides ($NiCo\text{-}MnO_2$) and nickel foam at a scan rate of 1 mVs^{-1}.

the ion exchange mechanism [55,56]. In this case, if the current density is low, the OH^- has enough time to interact with the surface of electrode which will be intercalated/extracted into/out of the electrode when charging/discharging occurs and hence a high specific capacity/capacitance is obtained. However, if the current density is high, less charge is transferred between electrolyte and the surface of electrode and hence a low specific capacity/capacitance is obtained.

Fig. 9 (d) shows the specific capacity retention and energy efficiency of a NiCo-MnO_2 electrode as a function of cycle number over 2000 charge-discharge cycles. The discharge capacity of approximately 66.3 mAh g^{-1} was retained for the half-cell electrode over 2000 charge-discharge cycles with an energy efficiency of about 93.3% compared to 48.2 % and 76.48 % respectively, for $NiCo(OH)_2$ electrode as shown in Fig. 9 (e). The high capacity retention of 66.3% could be ascribed to the higher electronic conductivity, due to the low R_s value (0.98 Ω). Besides, the particular porous and stacked sheet-like structure of NiCo-MnO_2 electrode makes the material much more accessible for ion diffusion in the interlayer sheets [57]. In addition, the electrochemical reactions usually depend on the insertion-extraction of OH^- from the electrolyte, while the porous structure is beneficial for the ions to diffuse into the electrode holes [58].

Moreover, compared with the previous studies available on the electrochemical performances of transition metal hydroxides-based electrodes and some manganese oxide-based electrodes evaluated in a three-electrode cell configuration [8,59,60], the NiCo-MnO_2 electrode displays the highest specific capacitance as shown in bar chat in Fig. 10.

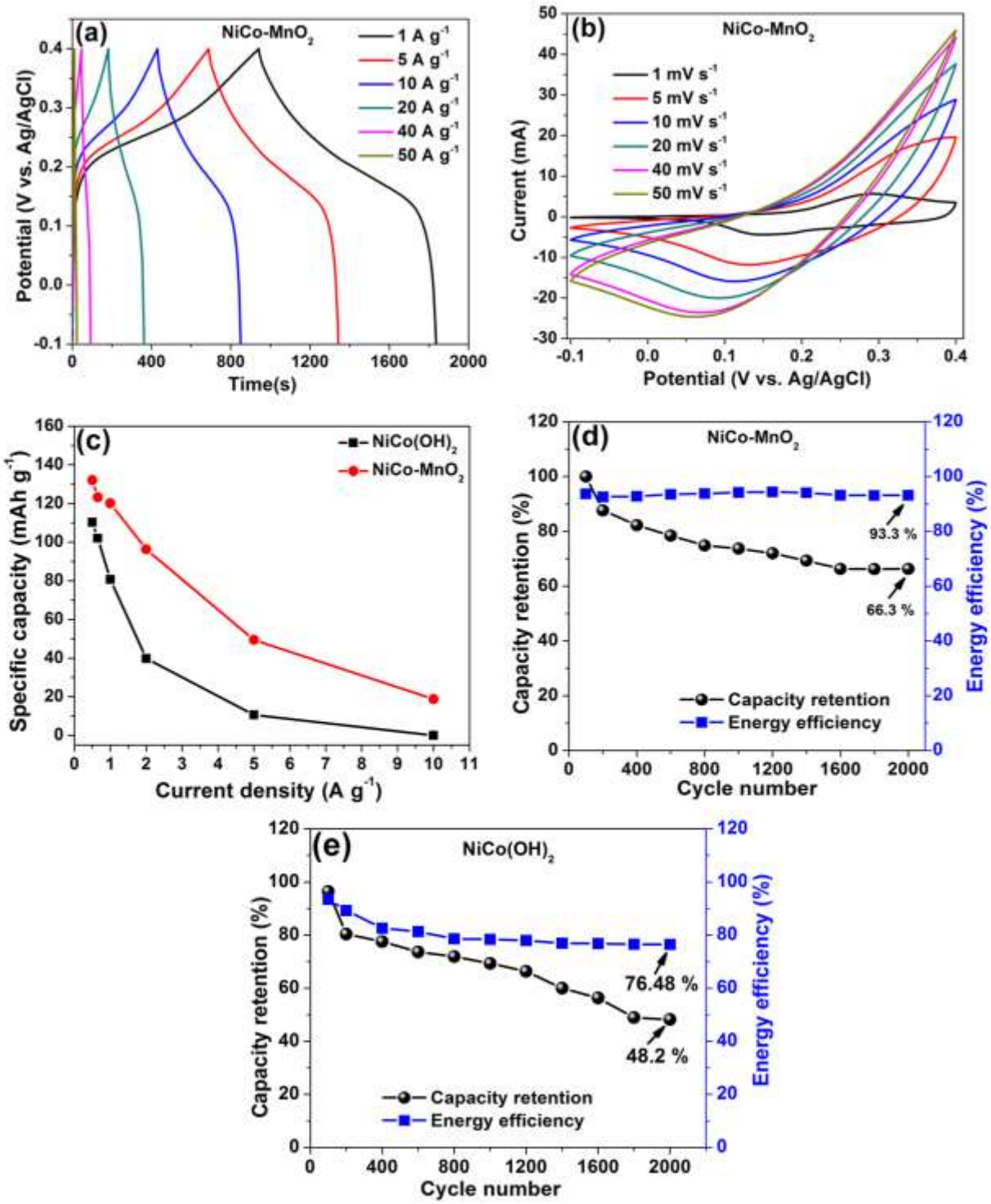

Fig. 9. (a) CD curves of NiCo-MnO_2 at different current densities, (b) the CV curves of NiCo-MnO_2 at various scan rates. (c) A plot of specific capacity against current densities for both $NiCo(OH)_2$ and NiCo-MnO_2. (d and e) Variations of specific capacity and energy efficiency of NiCo-MnO_2 and $NiCo(OH)_2$ electrodes as a function of cycle number measured at 5 A g^{-1} in 1 M KOH aqueous solution respectively.

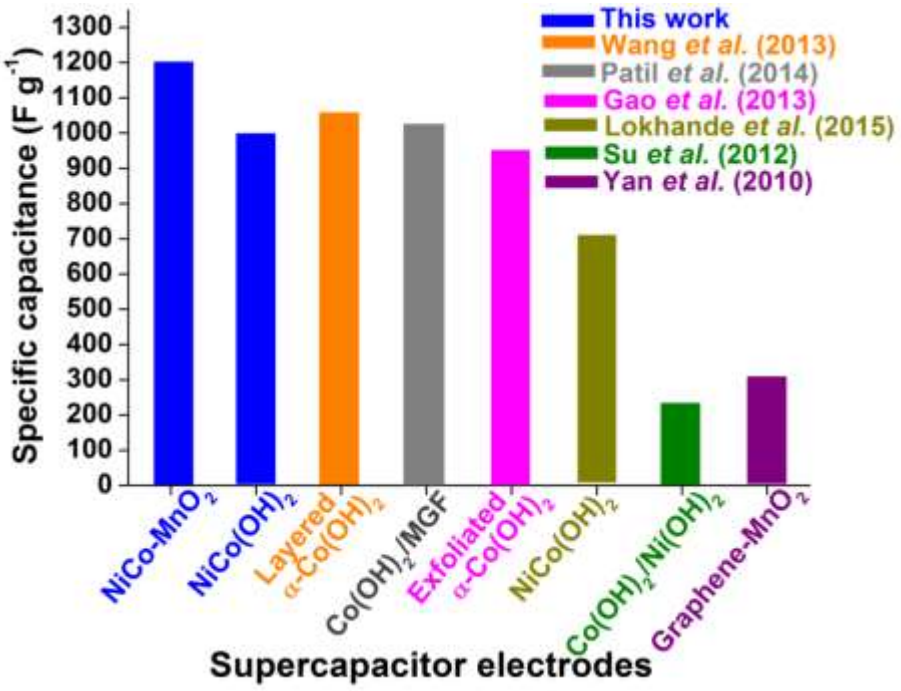

Fig. 10. A comparison of the specific capacitance of transition metal hydroxides-based electrodes and manganese oxide electrode evaluated in a three-electrode cell configuration found in this work and previously published results.

To further evaluate the electrical resistance of the $NiCo(OH)_2$ and $NiCo\text{-}MnO_2$ electrodes, the electrochemical impedance spectroscopy (EIS) at the potential of 0.0 V and the frequency range of 10 mHz –100 kHz was carried out. Fig. 11 (a) shows the Nyquist impedance plot of both $NiCo(OH)_2$ and $NiCo\text{-}MnO_2$. It can be observed that the Nyquist plots for both electrodes have distinct semicircle in the high frequency region which is attributed to the interfacial charge transfer resistance and mass transport through the material and is denoted by R_1, R_2 and R_3 respectively. In the Nyquist plot, the intersection with the real Z' axis is ascribed to the total resistance of the ionic resistance of electrolyte, the intrinsic resistance of the active materials and the contact resistance at the interface between the active electrode material and current collector [61], denoted as R_S. From the Fig. 11 (a), the R_S values for both $NiCo(OH)_2$ and $NiCo\text{-}MnO_2$ electrodes are 5.0 Ω and 0.98 Ω respectively.

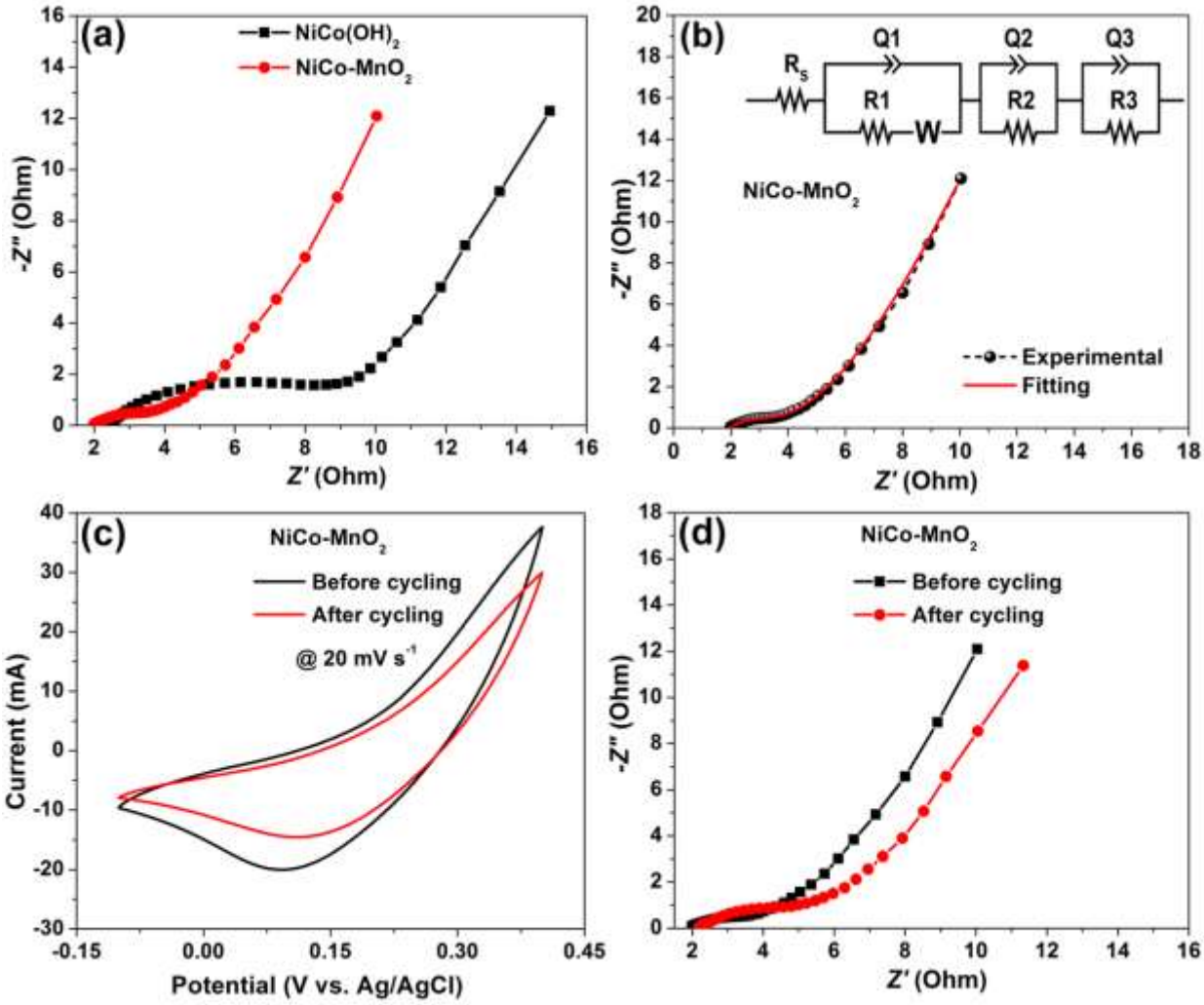

Fig. 11. (a) Nyquist impedance plot of both $NiCo(OH)_2$ and $NiCo\text{-}MnO_2$ electrodes. (b) fitted Nyquist plot of $NiCo\text{-}MnO_2$ electrode and the equivalent circuit (insert). (c) CV curves of $NiCo\text{-}MnO_2$ electrode before and after 2000 charge-discharge cycles at a scan rate of 20 mVs^{-1} and (d) Nyquist plots of $NiCo\text{-}MnO_2$ electrode before and after 2000 charge-discharge cycles at a current density of 5 A g^{-1}.

Interestingly, the low R_S value of the $NiCo\text{-}MnO_2$ electrode suggests high electrical conductivity, which results in the good capacitive performance of the electrode material. Furthermore, the Nyquist plot for $NiCo\text{-}MnO_2$ electrode was fitted (Fig. 11 (b)) using a ZFIT fitting program v11.02 with the equivalent circuit shown as inset to Fig. 11 (b). In the equivalent circuit, the R_S is connected in series with three units within the circuit, namely; the constant phase element, Q_1, which is connected in parallel with the charge transfer resistance, R_1. The transition from high-low frequency region is modeled by Warburg diffusion element and represented by W which is

in series with R_1. The second and third branch composed of another constant phase elements Q_2 and Q_3 which are non-intuitive circuit elements used in place of a capacitance in the series circuit with the resistance, and are connected in parallel with single resistance, R_2 and R_3 respectively. These two final branches represent the middle and low frequency region respectively. The incorporation of constant phase elements in the circuit can be ascribed to a distribution of the relaxation times owing to inhomogeneity occurring at the electrode/electrolyte interface, as well as the porous nature of the electrode material. Fig. 11 (c) shows the CV curves of NiCo-MnO_2 electrode before and after 2000 charge-discharge cycles at a scan rate of 20 mV s^{-1}. It can be seen that the current response of the NiCo-MnO_2 electrode after stability slightly decreased and this can be correlated to the increased resistance (i.e., semicircle in the high frequency region) as suggested by Fig. 11 (d).

The electrochemical properties of the as-synthesized C-FP were as well investigated for its use as a negative electrode in the hybrid asymmetric NiCo-MnO_2//C-FP supercapattery. The C-FP electrode was adopted as a potential negative electrode due to its ability to function effectively in the negative potential window. Fig. S4 displays the electrochemical performance of the C-FP electrode in 1 M KOH aqueous electrolyte at different scan rates in a three-electrode configuration. The C-FP -based negative electrode displayed no noticeable peaks in its curves, with an ideal rectangular CV curves, showing the material's double-layer capacitive characteristics with good reversibility. The EIS deduction has been one of the requisite techniques in probing the electrochemical behavior of electrode materials for supercapacitor. Fig. S4 (c) in the supplementary information shows the Nyquist plot of C-FP negative electrode used for the *SC*. The inset to the figure shows a low equivalent series resistance, R_s value of 0.92 Ω which is the intercept of the plot with the real *Z*'-axis at the high frequency region.

Fig. S4 (d) displays the specific capacitance values as a function of varying gravimetric current densities. Different C_S-values of 264.1, 224.1, 173.3, 155.0, 143.3, and 133.3 F g^{-1} at current

densities of 0.5, 1.0, 2.0, 3.0, 4.0 and 5.0 A g^{-1} respectively (see Fig. S4 (d)) were recorded for the C-FP negative electrode between -1.2 V to 0 V potential range.

The unique coulombic efficiency improvement (102.6%) after being subjected to cyclic stability test shown in Fig. S4 (e) could be ascribed to a good electronic conductivity and the crystalline nature of the C-FP material. This is confirmed from the observed nanostructured morphology of the C-FP from the SEM micrograph (Fig. S2 (a-b)), the sample TEM micrographs (Fig. S2 (c-d)), as well as the XRD analysis result of the carbon-based material (Fig. S3 (a)). The C-FP electrode also displayed good electrical conductivity as implied from EIS results (Fig. S4 (c)).

3.2.2. Two-electrode electrochemical measurements of the hybrid asymmetric NiCo-MnO_2//C-FP supercapattery

As a result of the remarkable electrochemical performances of both the positive and negative materials in Section 3.2.1., a hybrid asymmetric supercapattery, *SC* was fabricated and designated as NiCo-MnO_2//C-FP with mass balance ratio estimated according to equation 9, as 2.0: 3.34 corresponding to a loading mass of approximately 2.2 and 3.6 mg cm^{-2} for both NiCo-MnO_2 and C-FP selected as positive and negative electrode materials respectively, since the heightened sensitivity of a three-electrode configuration could over-project the storage capability of an electrode material for practical supercapacitor use. The NiCo-MnO_2 positive working electrode was prepared by mixing active material, carbon acetylene black as a conducting agent and polyvinylidenedifluoride (PVDF) as binder in a small amount of NMP solvent, in a weight ratio of 80:10:10 and was then coated onto the Ni foam current collector and dried overnight at 60 $^{\circ}$C under ambient environment. The total mass loading of both NiCo-MnO_2 and C-FP active materials in the hybrid asymmetric *SC* electrodes was estimated to be approximately 5.8 mg/cm^{-2}, with the electrode thickness of about 96 µm by means of micro balance. The electrochemical

testing of the asymmetric supercapacitor was carried out in two-electrode configurations using 1 M KOH aqueous electrolyte.

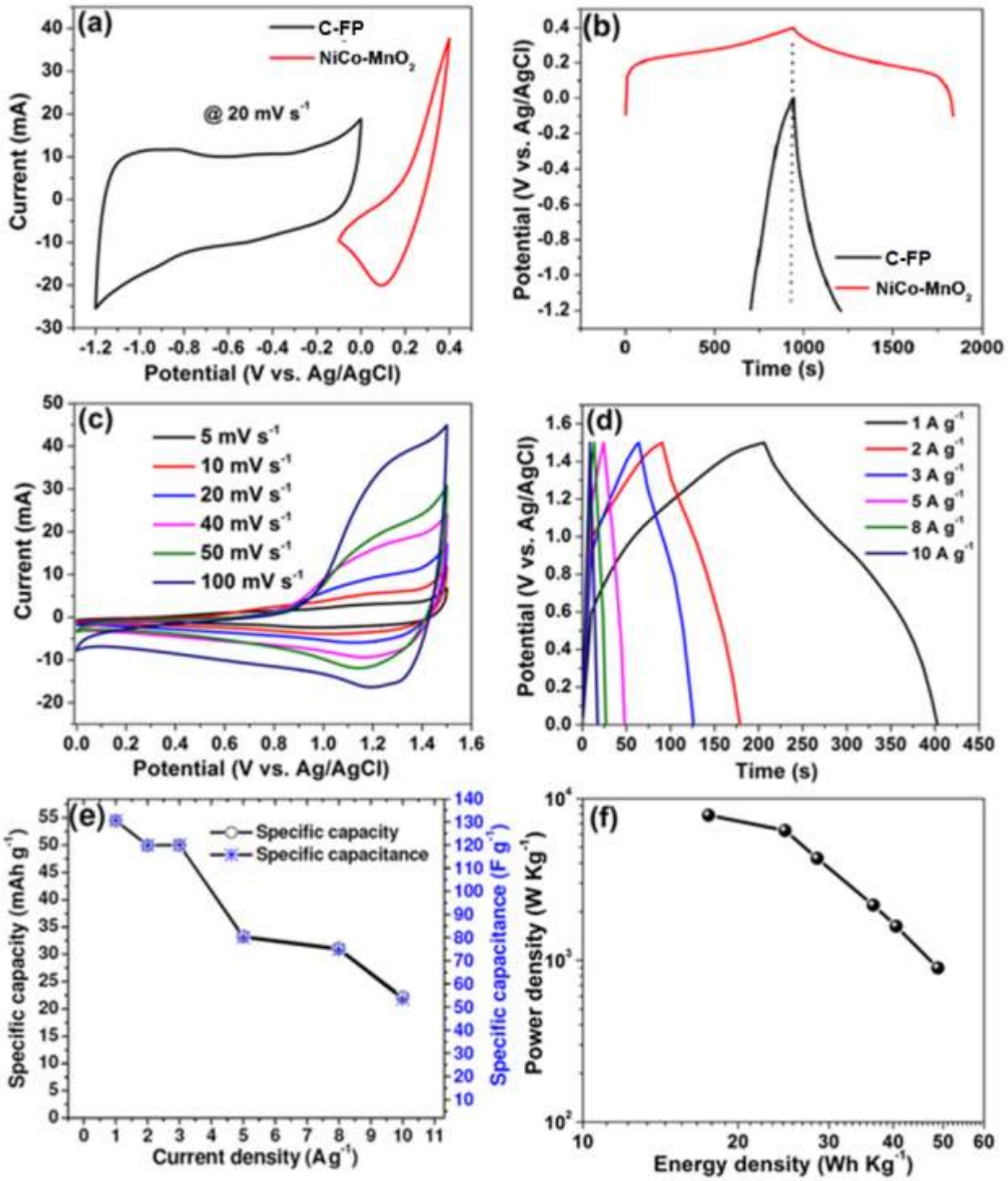

Fig. 12. (a) CV curves of NiCo-MnO_2 and C-FP at 20 mVs^{-1}, (b) CD profiles of NiCo-MnO_2 and C-FP at 1 Ag^{-1}, (c) CV curves of NiCo-MnO_2//C-FP at various scan rates, (e) specific capacity/capacitance of NiCo-MnO_2//C-FP determined at various current densities and (f) Ragone plots of the asymmetric device.

Fig. 12 (a) displays the individual CV profiles of the ternary NiCo-MnO_2 and C-FP electrodes at a scan rate of 20 mVs^{-1} in a three electrode configurations. The C-FP electrode exhibits a quasi-rectangular CV curve, which is quite close to the electric double-layer capacitive properties. It can be observed that the fabricated hybrid asymmetry *SC* could operate in a much wider potential window ~1.5 V based on the synergy of their respective operating potential limits. Fig. 12 (b) shows the associated CD profiles of NiCo-MnO_2 and C-FP at a 1 A g^{-1} current density. As expected, the CD profile for the ternary oxide is faradic in nature while the C-FP electrode displayed a much linear discharge characteristic confirming the double-layer capacitive trend.

Fig. 12 (c) shows the CV curves of the hybrid NiCo-MnO_2//C-FP asymmetric cell measured at various scan rates from 5 to 100 mV s^{-1}. It can be observed that the CV curves at various scan rates displayed a mixed electric-double layer capacitance and faradic behaviors which is typical of hybrid asymmetric *SC* [30]. Fig. 12 (d) displays the charge–discharge profiles of the hybrid asymmetric *SC* at various current densities. The triangular profiles are considerably non-symmetrical, indicating the contribution from the hybrid NiCo-MnO_2//C-FP *SC* redox reaction [30,57]. This is in accordance with the CV curves of the hybrid asymmetric device (Fig. 12 (c)).

Fig. 12(e) displays the hybrid asymmetric cell specific capacitance calculated using equation 5 and plotted as a function of current density. At a current density of 1 A g^{-1}, the hybrid cell was observed to deliver specific capacitance of 130.67 F g^{-1} corresponding to specific capacity of 54.45 mA h g^{-1}. Fig. 12 (f) displays the Ragone plot for both energy density and power density as two crucial parameters to determining the electrochemical behavior of the hybrid *SC*. The corresponding energy and power densities of the device were determined according to equations 6 and 7. The energy density of the hybrid *SC* was observed to reach as high as 48.83 Wh kg^{-1} corresponding to a power density of 896.88 W kg^{-1} at a current density of 1 A g^{-1}. Interestingly, at a power density of 6345 W kg^{-1}, the energy density remained as high as 24.675 Wh kg^{-1} at a

current density of 8 A g^{-1}. This hints that the fabricated asymmetric *SC* could dispense a high power density devoid of a considerable loss in the stored energy. This point addresses the important fact that as much as the goal in the supercapacitor research is improve its energy density to match that of batteries, this is not supposed to be done at the expense of a compromised power density of the SC.

The energy densities recorded by the hybrid *SC* showed considerable improvement when compared to other asymmetric *SCs* in aqueous electrolyte. Such as, FeOOH//MnO_2; 24 Wh kg^{-1} at power density of 3700 W kg^{-1}, at 0.5 A g^{-1}[62], MnO_x//graphene; 23.02 Wh kg^{-1} at power density of 947 W kg^{-1}, at 1 A g^{-1}[63], MnS//EDAC; 37.6 Wh kg^{-1} at power density of 181.2 W kg^{-1}, at 1 A g^{-1}[57], C7N3//AC; 34.9 Wh kg-1 at power density of 875 W g^{-1}, at 1 A g^{-1}[50]; AEG//PAC; 24.6 Wh kg^{-1} at power density of 400 W kg^{-1}, at 0.5 A g^{-1}[64] and AC//RGO-CoO; 35.7 Wh kg^{-1} at power density of 225 W kg^{-1}, at 0.5 A g^{-1}[65]. A maximum constant-current discharge power density of 440.83 kW kg^{-1} was recorded as determined according to equation 8 for the hybrid asymmetric *SC*.

From Fig. 13 (a), it could be observed that the hybrid *SC* records an excellent coulombic efficiency of 99.98 % (using ES1) and as well preserves 96.78% of its incipient capacitance up to a 10000 constant charge-discharge cycle at a current density of 3 A g^{-1}. Such impressive stability is mostly seen for EDLC and not supercapattery-type devices. This unique behaviour is due to the mesoporous structure that could play an important role in heightening the effective electrode surface area, facilitating electrolyte permeation, and shortening the electron pathway in the active materials [57]. The mesoporous structure of the ternary NiCo-MnO_2 nanocrystal is better accessible for the reactant molecules cum cations via the interlayer space [66]. Moreover, the particular mesoporous structure could accommodate well the solvated ions (OH^-), thereby contributing to capacitance enhancement owing to compact layers of ions residing on both adjacent hole walls [57,67].

The mesoporous structure could bring about ion and electron transfer, restraining the volumetric alteration of the electrode in the charge-discharge process [50].

Electrochemical impedance spectroscopy (EIS) analysis was used to further confirm the electrochemical behaviour of the device (Fig. 13 (b & d)). Fig. 13 (b) is a display of the Nyquist plot with a fit using the equivalent circuit inset to the Figure. The solution resistance, R_s and charge transfer resistance, R_{CT} were estimated to be 0.22 Ω and 1.94 Ω, respectively, which are significantly smaller compared with what is obtainable in the literature [57,64], indicating the desirable electrical properties of the materials used in the hybrid *SC*. The R_{CT} of NiCo-MnO_2 electrode portrays charge-transfer resistance, while the R_{CT} of C-FP is liable for the self-discharge process [13,57]. At the high frequency, the equivalent series resistance, R_s which is the intercept to the *Z*'-axis, includes the total resistance comprising the electrolyte resistance, and the resistance between the contact and the electrode materials. The calculated values of R_s, R_{CT}, and Q using ZFIT program software are summarized in Table S1 in the supplementary information.

At the mid-frequency region, a small semicircle, designated as R_{CT} is noticed owing to the charge transfer resistance and mass transport across the framework of the material. At the low-frequency region, the curve portrays a line fairly perpendicular to the *Z*"-axis marking an ideal behavior of the hybrid *SC*. The device nevertheless, shows a divergence from this ideal behaviour owing to a resistive element, R_L (leakage current resistance) associated and in parallel with constant phase element, Q_2.

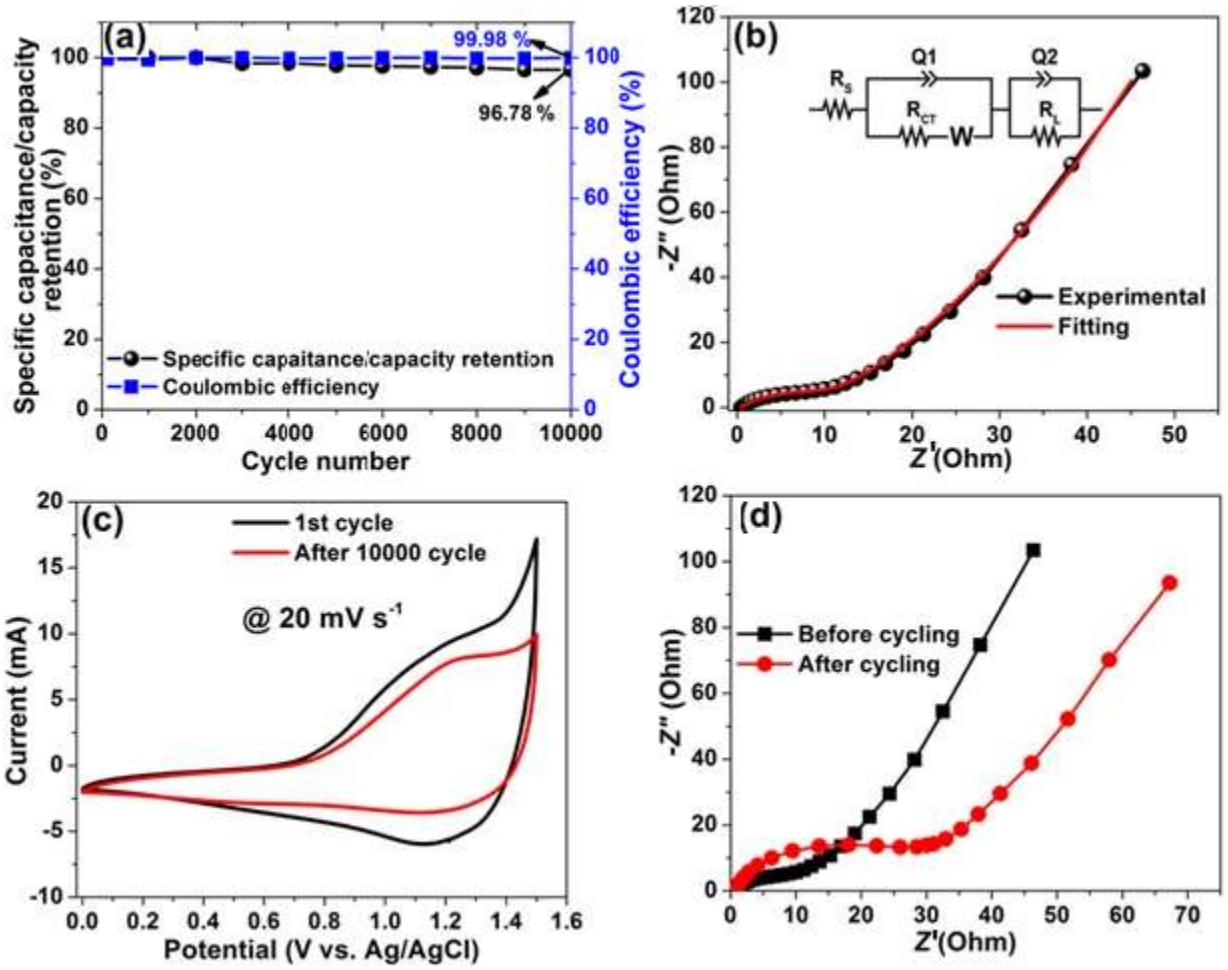

Fig. 13. (a) cyclic performance, (b) EIS plot and fitting curve, (c) CV curves before and after cycling for the hybrid asymmetric *SC* respectively and (d) EIS before and after 10000 cycling of the hybrid NiCo-MnO_2//C-FP asymmetric device at a current density of 3 Ag^{-1}.

The deviation from the perfect line perpendicular to the *Z*''-axis is as a result of a diffusion process which occurs at the electrode-electrolyte interface, mainly indicated by the existence of a Warburg impedance element, *W* [68]. By standard, the phase angle of the Warburg impedance is -45°, being a representation of a vector of equal real and imaginary amplitudes. In practice, a deviation from that phase angle is noticed and is attributed to porous nature of the electrode materials with different pore dimensions which play an important role in the impedance analysis [69]. The transition from high to low frequency is represented by Warburg element (*W*) which is

in series with R_{ct}. In principle, an ideal cell will give a vertical line parallel to the y-axis at a low frequency which is represented by constant phase element, Q_1 in the circuit diagram.

Fig. 13 (c) shows the CV curves of the hybrid *SC* before and after 10000 cycling at a scan rate of 20mVs^{-1}. It can be seen that even after a very large number of cycles, the current response of the NiCo-MnO_2//C-FP hybrid *SC* after stability slightly decreased while the shape is still preserved which shows the relative stability of cell for potential practical application. Fig. 13 (d) shows the Nyquist plot of the device before and after 10000 cycles. After cycling, the diffusion path length is observed to further deviate from the ideal vertical nature which can be ascribed to the repeated cycling effects such as polarization and less utilization or insufficient active material during redox reaction, probably owing to the high current density [11].

Fig. S4 (f) displays the self-discharge (SD) profile of the hybrid NiCo-MnO_2//C-FP symmetric *SC* carried out at room temperature in 1 M KOH electrolyte. The cell was charged to its peak voltage of 1.50 V at 0.5 A g^{-1} and then held at that voltage for about 1 h and later kept at open circuit potential to undergo self-discharge for more than 50 h with the *SC's* terminals' voltage being monitored. The *SC* was observed to maintain a substantial voltage of 1.11 V (over 74% of its operating voltage) which indicates a good practical application of the hybrid *SC*. The sudden fall of the hybrid *SC* voltage at the incipient stage of the self-discharge is perhaps as a result of the decomposition of water used as the solvent, as previously explained [70,71]. Concisely, when the cell is fully charged, the solvent could be abridged on the cathode, a reduction that could continue even after current cut-off, resulting in a sharp decrease in the cathode potential [64]. This procedure is influenced by the surface property of the electrode and is not diffusion controlled neither due to current leakage. Accordingly, any investigation of the self-discharge mechanism will exclude the potential drop [64,70].

4. CONCLUSION

Mixed transition meta hydroxides $NiCo(OH)_2$, NiCoMn-triple hydroxide (NiCoMn-TH) and a ternary NiCo-MnO_2 electrode materials were successfully synthesised by force-driven hydrolysis of hydrated nitrates of nickel, cobalt and manganese salt at a low temperature while C-FP electrode was synthesized via a complete dissolution of iron (III) nitrate and PANI in ethanol. The characterization of the samples confirmed that the as-prepared mixed hydroxides electrode materials have agglomerated flake-like particles which exhibited a small specific surface area compared to the NiCo-MnO_2 with porous and stacked sheet-like morphology. It was also confirmed that the prepared samples are crystalline, and composed of Ni, Co, O (or O–H bond in $NiCo(OH)_2$ sample) and Mn in NiCo-MnO_2 sample with Ni, Co and Mn existing in different oxidation states. The C-FP on the other hand, is composed of nano grains with some level of crystallinity. The electrochemical performance of the electrode materials evaluated in a three-electrode cell configuration using 1 M KOH electrolyte showed a significant improvement on specific capacity of 132.1 mAh g^{-1} for NiCo-MnO_2 compared to 110.3 and 64.36 mAh g^{-1} for $NiCo(OH)_2$ and the unstable NiCoMn-TH at a current density of 0.5 A g^{-1} respectively. The C-FP electrode showed a good and consistent capacitive performance with relatively high specific capacitance of 264.17 Fg^{-1} at a current density of 0.5 A g^{-1} in KOH aqueous electrolyte. A cost-effective high-performance hybrid NiCo-MnO_2//C-FP supercapattery in 1 M KOH electrolyte delivered a high energy density of 48.83 Wh kg^{-1} with a corresponding high power density of 896.88 W kg^{-1} as well as excellent stability with 97.78% capacity retention up to 10,000 cycles similar to what is observed in classic EDLC devices. Even at high current density of 8 A g^{-1} the device maintained a high energy density of 25 Wh kg^{-1} with corresponding power density of 6344 W kg^{-1} which shows that these are excellent materials for supercapacitor applications.

ACKNOWLEDGEMENTS

This work is based on the research supported by the South African Research Chairs Initiative of the Department of Science and Technology and National Research Foundation of South Africa (Grant No. 61056). Any opinion, finding, and conclusion expressed in this material are that of the author(s), and the NRF does not accept any liability in this regard. K. O. Oyedotun acknowledges financial support from the University of Pretoria and National Research Foundation (NRF) for his PhD studies.

REFERENCES

[1] R.R. Salunkhe, J. Lin, V. Malgras, S.X. Dou, J.H. Kim, Y. Yamauchi, Large-scale synthesis of coaxial carbon nanotube/Ni(OH)2 composites for asymmetric supercapacitor application, Nano Energy. 11 (2015) 211–218, doi:10.1016/j.nanoen.2014.09.030.

[2] R.R. Salunkhe, C. Young, J. Tang, T. Takei, Y. Ide, N. Kobayashi, Y. Yamauchi, A high-performance supercapacitor cell based on ZIF-8-derived nanoporous carbon using an organic electrolyte, Chem. Commun. 52 (2016) 4764–4767, doi:10.1039/C6CC00413J.

[3] N.L. Torad, R.R. Salunkhe, Y. Li, H. Hamoudi, M. Imura, Y. Sakka, C.C. Hu, Y. Yamauchi, Electric double-layer capacitors based on highly graphitized nanoporous carbons derived from ZIF-67, Chem. - A Eur. J. 20 (2014) 7895–7900, doi:10.1002/chem.201400089.

[4] R.R. Salunkhe, Y.V. Kaneti, J. Kim, J.H. Kim, Y. Yamauchi, Nanoarchitectures for Metal-Organic Framework-Derived Nanoporous Carbons toward Supercapacitor Applications, Acc. Chem. Res. 49 (2016) 2796–2806, doi:10.1021/acs.accounts.6b00460.

[5] M. Armand, J.-M. Tarascon, Building better batteries, Nature. 451 (2008) 652–657, doi:10.1038/451652a.

[6] F. Zhang, T. Zhang, X. Yang, L. Zhang, K. Leng, Y. Huang, Y. Chen, A high-performance supercapacitor-battery hybrid energy storage device based on graphene-enhanced electrode materials with ultrahigh energy density, Energy Environ. Sci. 6 (2013) 1623, doi:10.1039/c3ee40509e.

[7] J. Xu, S. Dou, H. Liu, L. Dai, Cathode materials for next generation lithium ion batteries, *2* (4) (2013) 439-442, doi:10.1016/j.nanoen.2013.05.013.

[8] P.E. Lokhande, Synthesis and Characterization of Ni.Co(OH) 2 Material for Supercapacitor Application, Int. Adv. Res. J. Sci. Eng. Technol. 2 (9) (2015) 10-13, doi:10.17148/IARJSET.2015.2903.

[9] X. Wang, X. Fan, G. Li, M. Li, X. Xiao, A. Yu, Z. Chen, Composites of MnO2 nanocrystals and partially graphitized hierarchically porous carbon spheres with improved rate capability for high-performance supercapacitors, Carbon N. Y. 93 (2015) 258–265, doi:10.1016/j.carbon.2015.05.072.

[10] H.D. Abruna, Y. Kiya, J.C. Henderson, Batteries and Electrochemical Capacitors, Phys. Today. 61 (12) (2008) 43–47, doi: 10.1063/1.3047681.

[11] K.O. Oyedotun, M.J. Madito, A. Bello, D.Y. Momodu, A.A. Mirghni, N. Manyala, Investigation of graphene oxide nanogel and carbon nanorods as electrode for electrochemical supercapacitor, Electrochim. Acta. 245 (2017) 268–278, doi:10.1016/j.electacta.2017.05.150.

[12] P.U. Asogwa, S.C. Ezugwu, F.I. Ezema, Variation of optical and solid state properties with post deposition annealing in PVA-Capped MnO_2 thin films, Superf. Y Vacío. 23 (2010) 18–22, http://smcsyv.fis.cinvestav.mx/supyvac/23_1/SV2311810.

[13] P. Simon, Y. Gogotsi, Materials for electrochemical capacitors, Nat. Mater. 7 (2008) 845–854, doi:10.1038/nmat2297.

[14] I. Hadjipaschalis, A. Poullikkas, V. Efthimiou, Overview of current and future energy storage technologies for electric power applications, Renew. Sustain. Energy Rev. 13 (2009) 1513–1522, doi:10.1016/j.rser.2008.09.028.

[15] J.P. Cheng, J. Zhang, F. Liu, Recent development of metal hydroxides as electrode material of electrochemical capacitors, RSC Adv. 4 (2014) 38893–38917, doi:10.1039/C4RA06738J.

[16] W. Zhang, F. Liu, Q. Li, Q. Shou, J. Cheng, L. Zhang, B.J. Nelson, X. Zhang, Transition metal oxide and graphene nanocomposites for high-performance electrochemical capacitors, Phys. Chem. Chem. Phys. 14 (2012) 16331–16337, doi:10.1039/C2CP43673F.

[17] G. Wang, L. Zhang, J. Zhang, A review of electrode materials for electrochemical

supercapacitors, Chem. Soc. Rev. 41 (2012) 797–828, doi:Doi 10.1039/C1cs15060j.

[18] H. Chen, L. Hu, Y. Yan, R. Che, M. Chen, L. Wu, One-step fabrication of ultrathin porous nickel hydroxide-manganese dioxide hybrid nanosheets for supercapacitor electrodes with excellent capacitive performance, Adv. Energy Mater. 3 (2013) 1636–1646, doi:10.1002/aenm.201300580.

[19] H. Chen, L. Hu, Y. Yan, R. Che, M. Chen, L. Wu, One-step fabrication of ultrathin porous nickel hydroxide-manganese dioxide hybrid nanosheets for supercapacitor electrodes with excellent capacitive performance, Adv. Energy Mater. 3 (2013) 1636–1646, doi:10.1002/aenm.201300580.

[20] L. Feng, Y. Zhu, H. Ding, C. Ni, Recent progress in nickel based materials for high performance pseudocapacitor electrodes, J. Power Sources. 267 (2014) 430–444, doi:10.1016/j.jpowsour.2014.05.092.

[21] T. Deng, W. Zhang, O. Arcelus, J.-G. Kim, J. Carrasco, S.J. Yoo, W. Zheng, J. Wang, H. Tian, H. Zhang, X. Cui, T. Rojo, Atomic-level energy storage mechanism of cobalt hydroxide electrode for pseudocapacitors, Nat. Commun. 8 (2017) 15194, doi:10.1038/ncomms15194.

[22] Z. Pan, Y. Qiu, J. Yang, F. Ye, Y. Xu, X. Zhang, M. Liu, Y. Zhang, Ultra-endurance flexible all-solid-state asymmetric supercapacitors based on three-dimensionally coated MnOx nanosheets on nanoporous current collectors, Nano Energy. 26 (2016) 610–619, doi:10.1016/j.nanoen.2016.05.053.

[23] H.X. Wang, W. Zhang, N.E. Drewett, H.B. Zhang, K.K. Huang, S.H. Feng, X.L. Li, J. Kim, S. Yoo, T. Deng, S.J. Liu, D. Wang, W.T. Zheng, Unifying miscellaneous performance criteria for a prototype supercapacitor via Co(OH)2 active material and current collector interactions, J. Microsc. 267 (2017) 34–48, doi:10.1111/jmi.12545.

[24] C. Zhang, K.B. Hatzell, M. Boota, B. Dyatkin, M. Beidaghi, D. Long, W. Qiao, E.C. Kumbur, Y. Gogotsi, Highly porous carbon spheres for electrochemical capacitors and capacitive flowable suspension electrodes, Carbon N. Y. 77 (2014) 155–164, doi:10.1016/j.carbon.2014.05.017.

[25] G. Godillot, L. Guerlou-Demourgues, P.-L. Taberna, P. Simon, C. Delmas, Original Conductive Nano-Co3O4 Investigated as Electrode Material for Hybrid Supercapacitors, Electrochem. Solid-State Lett. 14 (2011) A139, doi:10.1149/1.3609259.

[26] B. Akinwolemiwa, C. Peng, G.Z. Chen, Redox Electrolytes in Supercapacitors, J. Electrochem. Soc. 162 (2015) A5054–A5059, doi:10.1149/2.0111505jes.

[27] B.E. Conway, Electrochemical supercapacitors: scientific fundamentals and technological applications, Springer Science & Business Media, (2013), doi:10.1007/978-1-4757-3058-6.

[28] A. Burke, Ultracapacitors: Why, how, and where is the technology, J. Power Sources. 91 (2000) 37–50, doi:10.1016/S0378-7753(00)00485-7.

[29] J. Zhang, J.P. Cheng, M. Li, L. Liu, F. Liu, X.B. Zhang, Flower-like nickel-cobalt binary hydroxides with high specific capacitance: Tuning the composition and asymmetric capacitor application, J. Electroanal. Chem. 743 (2015) 38–45, doi:10.1016/j.jelechem.2015.02.021.

[30] T.M. Masikhwa, M.J. Madito, D.Y. Momodu, J.K. Dangbegnon, O. Guellati, A. Harat, M. Guerioune, F. Barzegar, N. Manyala, High performance asymmetric supercapacitor based on CoAl-LDH/GF and activated carbon from expanded graphite, RSC Adv. 6 (2016) 46723–46732, doi:10.1039/C6RA07419G.

[31] A. Szytula, A. Murasik, M. Balanda, Neutron Diffraction Study of Ni(OH)2, Phys. Status Solidi. 43 (1971) 125–128, doi:10.1002/pssb.2220430113.

[32] T. Takada, Y. Bando, M. Kiyama, H. Miyamoto, T. Sato, The Magnetic Property of β-$Co(OH)_2$, J. Phys. Soc. Japan. 21 (1966) 2726–2726, doi:10.1143/JPSJ.21.2726.

[33] C. Zhao, X. Wang, S. Wang, Y. Wang, Y. Zhao, W. Zheng, Synthesis of Co(OH) 2/graphene/Ni foam nano-electrodes with excellent pseudocapacitive behavior and high cycling stability for supercapacitors, Int. J. Hydrogen Energy. 37 (2012) 11846–11852, doi:10.1016/j.ijhydene.2012.05.138.

[34] W. Zhou, X. Cao, Z. Zeng, W. Shi, Y. Zhu, Q. Yan, H. Liu, J. Wang, H. Zhang, One-step synthesis of Ni_3S_2 nanorod@$Ni(OH)_2$ nanosheet core–shell nanostructures on a three-dimensional graphene network for high-performance supercapacitors, Energy Environ. Sci. 6 (2013) 2216–2221, doi:10.1039/C3EE40155C.

[35] S.R. Shieh, T.S. Duffy, Raman spectroscopy of $Co(OH)_2$ at high pressures: Implications for amorphization and hydrogen repulsion, Phys. Rev. B. 66 (2002) 134301, doi:10.1103/PhysRevB.66.134301.

[36] H.D. Lutz, H. Möller, M. Schmidt, Lattice vibration spectra. Part LXXXII. Brucite-type hydroxides M(OH)2 (M = Ca, Mn, Co, Fe, Cd) — IR and Raman spectra, neutron diffraction of Fe(OH)2, J. Mol. Struct. 328 (1994) 121–132, doi:10.1016/0022-2860(94)08355-X.

[37] J. Yang, H. Liu, W.N. Martens, R.L. Frost, Synthesis and Characterization of Cobalt Hydroxide, Cobalt Oxyhydroxide, and Cobalt Oxide Nanodiscs, J. Phys. Chem. C. 114 (2010) 111–119, doi:10.1021/jp908548f.

[38] T. Pauporté, L. Mendoza, M. Cassir, M.C. Bernard, J. Chivot, Direct Low-Temperature Deposition of Crystallized CoOOH Films by Potentiostatic Electrolysis, J. Electrochem. Soc. 152 (2005) C49, doi:10.1149/1.1842044.

[39] H. Xia, Y. Wang, J. Lin, L. Lu, Hydrothermal synthesis of MnO_2 /CNT nanocomposite with a CNT core/porous MnO_2 sheath hierarchy architecture for supercapacitors, Nanoscale research letters, 7 (1) (2012) 33, doi:10.1186/1556-276X-7-33.

[40] A. Ogata, S. Komaba, R. Baddour-Hadjean, J.-P. Pereira-Ramos, N. Kumagai, Doping effects on structure and electrode performance of K-birnessite-type manganese dioxides for rechargeable lithium battery, Electrochim. Acta. 53 (2008) 3084–3093, doi:10.1016/j.electacta.2007.11.038.

[41] Y. Ren, N. Yan, J. Feng, J. Ma, Q. Wen, N. Li, Q. Dong, Adsorption mechanism of copper and lead ions onto graphene nanosheet/δ-MnO2, Mater. Chem. Phys. 136 (2012) 538–544, doi:10.1016/j.matchemphys.2012.07.023.

[42] Y. Zhao, H. Ma, S. Huang, X. Zhang, M. Xia, Y. Tang, Z.-F. Ma, Monolayer Nickel Cobalt Hydroxyl Carbonate for High Performance All-Solid-State Asymmetric Supercapacitors, ACS Appl. Mater. Interfaces. 8 (2016) 22997–23005, doi:10.1021/acsami.6b05496.

[43] R. Li, Z. Hu, X. Shao, P. Cheng, S. Li, W. Yu, W. Lin, D. Yuan, Large Scale Synthesis of NiCo Layered Double Hydroxides for Superior Asymmetric Electrochemical Capacitor, Sci. Rep. 6 (2016) 18737, doi:10.1038/srep18737.

[44] J. Pérez-Ramírez, G. Mul, F. Kapteijn, J.A. Moulijn, In situ investigation of the thermal decomposition of Co–Al hydrotalcite in different atmospheres, J. Mater. Chem. 11 (2001) 821–830, doi:10.1039/b009320n.

[45] P.R. Jothi, K. Shanthi, R.R. Salunkhe, M. Pramanik, V. Malgras, S.M. Alshehri, Y. Yamauchi, Synthesis and Characterization of α--$NiMoO_4$ Nanorods for Supercapacitor -Application, Eur. J. Inorg. Chem. 2015 (2015) 3694–3699, doi:10.1002/ejic.201500410.

[46] Y. Gao, L. Mi, W. Wei, S. Cui, Z. Zheng, H. Hou, W. Chen, Double Metal Ions Synergistic Effect in Hierarchical Multiple Sulfide Microflowers for Enhanced Supercapacitor Performance, 7 (7) (2015) 4311-4319, doi:10.1021/am508747m.

[47] X. Lu, X. Huang, S. Xie, T. Zhai, C. Wang, P. Zhang, M. Yu, W. Li, C. Liang, Y. Tong, Controllable synthesis of porous nickel–cobalt oxide nanosheets for supercapacitors, J. Mater. Chem. 22 (2012) 13357, doi:10.1039/c2jm30927k.

[48] H. Cheng, Y.-Z. Su, P.-Y. Kuang, G.-F. Chen, Z.-Q. Liu, Hierarchical $NiCo_2O_4$ nanosheet-decorated carbon nanotubes towards highly efficient electrocatalyst for water oxidation, J. Mater. Chem. A. 0 (2015) 1–8, doi:10.1039/C5TA03985A.

[49] S. Hu, Y. Li, F. Lai, X. Zhang, Q. Li, Y. Huang, X. Yuan, J. Chen, H. Wang, Enhanced electrochemical performance of $LiMn_2O_4$ cathode with a $Li_{0.34}La_{0.51}TiO_3$ -coated layer, RSC Adv. 5 (2015) 17592–17600, doi:10.1039/C4RA15374J.

[50] J. Zhang, F. Liu, J.P. Cheng, X.B. Zhang, Binary Nickel-Cobalt Oxides Electrode Materials for High-Performance Supercapacitors: Influence of its Composition and Porous Nature, ACS Appl. Mater. Interfaces. 7 (2015) 17630–17640, doi:10.1021/acsami.5b04463.

[51] M. Li, J.P. Cheng, J.H. Fang, Y. Yang, F. Liu, X.B. Zhang, NiAl-layered Double Hydroxide/Reduced Graphene Oxide Composite: Microwave-assisted Synthesis and Supercapacitive Properties, Electrochim. Acta. 134 (2014) 309–318, doi:10.1016/j.electacta.2014.04.141.

[52] D. Cai, B. Liu, D. Wang, Y. Liu, L. Wang, H. Li, Y. Wang, C. Wang, Q. Li, T. Wang, Facile hydrothermal synthesis of hierarchical ultrathin mesoporous NiMoO4 nanosheets for high performance supercapacitors, Electrochim. Acta. 115 (2014) 358–363, doi:10.1016/j.electacta.2013.10.154.

[53] M.-C. Liu, L. Kang, L.-B. Kong, C. Lu, X.-J. Ma, X.-M. Li, Y.C. Luo, Facile synthesis of $NiMoO_4$ xH 2 O nanorods as a positive electrode material for supercapacitors, RSC Advances 3 (18) (2013) 6472-6478, doi:10.1039/c3ra22993a.

[54] J.F. Marco, J.R. Gancedo, M. Gracia, J.L. Gautier, E.I. Rios, H.M. Palmer, C. Greaves, F.J. Berry, Cation distribution and magnetic structure of the ferrimagnetic spinel NiCo2O4, J. Mater. Chem. 11 (2001) 3087–3093, doi:10.1039/B103135J.

[55] S. Xiong, C. Yuan, X. Zhang, B. Xi, Y. Qian, Controllable synthesis of mesoporous Co3O4 nanostructures with tunable morphology for application in supercapacitors, Chem. - A Eur. J. 15 (2009) 5320–5326, doi:10.1002/chem.200802671.

[56] C. Yuan, X. Zhang, L. Su, B. Gao, L. Shen, Facile synthesis and self-assembly of hierarchical porous NiO nano/micro spherical superstructures for high performance supercapacitors, J. Mater. Chem. 19 (2009) 5772–5777, doi:10.1039/B902221J.

[57] T. Chen, Y. Tang, Y. Qiao, Z. Liu, W. Guo, J. Song, S. Mu, S. Yu, Y. Zhao, F. Gao, All-solid-state high performance asymmetric supercapacitors based on novel MnS nanocrystal and activated carbon materials, Sci. Rep. 6 (2016) 23289, doi:10.1038/srep23289.

[58] Y. Zhang, M. Ma, J. Yang, H. Su, W. Huang, X. Dong, Selective synthesis of hierarchical mesoporous spinel NiCo(2)O(4) for high-performance supercapacitors, Nanoscale. 6 (2014) 4303–4308, doi:10.1039/c3nr06564b.

[59] L. Wang, Z.H. Dong, Z.G. Wang, F.X. Zhang, J. Jin, Layered α-$Co(OH)_2$ Nanocones as Electrode Materials for Pseudocapacitors: Understanding the Effect of Interlayer Space on Electrochemical Activity, Adv. Funct. Mater. 23 (2013) 2758–2764, doi:10.1002/adfm.201202786.

[60] U.M. Patil, M.S. Nam, J.S. Sohn, S.B. Kulkarni, R. Shin, S. Kang, S. Lee, J.H. Kim, S.C. Jun, Controlled electrochemical growth of $Co(OH)_2$ flakes on 3D multilayered graphene foam for high performance supercapacitors, J. Mater. Chem. A. 2 (2014) 19075–19083, doi:10.1039/C4TA03953J.

[61] X.Y. Liu, Y.Q. Zhang, X.H. Xia, S.J. Shi, Y. Lu, X.L. Wang, C.D. Gu, J.P. Tu, Self-assembled porous $NiCo_2O_4$ hetero-structure array for electrochemical capacitor, J. Power Sources. 239 (2013) 157–163, doi:10.1016/j.jpowsour.2013.03.106.

[62] W.H. Jin, G.T. Cao, J.Y. Sun, Hybrid supercapacitor based on MnO_2 and columned FeOOH using Li_2SO_4 electrolyte solution, J. Power Sources. 175 (2008) 686–691, doi:10.1016/j.jpowsour.2007.08.115.

[63] J. Yang, G. Li, Z. Pan, M. Liu, Y. Hou, Y. Xu, H. Deng, L. Sheng, X. Zhao, Y. Qiu, Y.

Zhang, All-Solid-State High-Energy Asymmetric Supercapacitors Enabled by Three-Dimensional Mixed-Valent MnOx Nanospike and Graphene Electrodes, ACS Appl. Mater. Interfaces. 7 (2015) 22172–22180, doi:10.1021/acsami.5b07849.

[64] F. Barzegar, A. Bello, J.K. Dangbegnon, N. Manyala, X. Xia, Asymmetric carbon supercapacitor with activated expanded graphite as cathode and Pinecone tree activated carbon as anode materials, Appl. Energy. 0 (2016) 0–5, doi:10.1016/j.apenergy.2017.05.110.

[65] L.J. Xie, J.F. Wu, C.M. Chen, C.M. Zhang, L. Wan, J.L. Wang, Q.Q. Kong, C.X. Lv, K.X. Li, G.H. Sun, A novel asymmetric supercapacitor with an activated carbon cathode and a reduced graphene oxide-cobalt oxide nanocomposite anode, J. Power Sources. 242 (2013) 148–156, doi:10.1016/j.jpowsour.2013.05.081.

[66] A. Bergmann, I. Zaharieva, H. Dau, P. Strasser, Electrochemical water splitting by layered and 3D cross-linked manganese oxides: correlating structural motifs and catalytic activity, Energy Environ. Sci. 6 (2013) 2745, doi:10.1039/c3ee41194j.

[67] E. Raymundo-Pinero, P. Azais, T. Cacciaguerra, D. Cazorla-Amorós, A. Linares-Solano, F. Béguin, KOH and NaOH activation mechanisms of multiwalled carbon nanotubes with different structural organisation, Carbon. 43 (4) (2005) 786–795, doi:10.1016/j.carbon.2004.11.005.

[68] H. Li, J. Wang, Q. Chu, Z. Wang, F. Zhang, S. Wang, Theoretical and experimental specific capacitance of polyaniline in sulfuric acid, J. Power Sources. 190 (2009) 578–586, doi:10.1016/j.jpowsour.2009.01.052.

[69] H. Song, H. Song, Y. Jung, Y. Jung, K. Lee, K. Lee, L.H. Dao, L.H. Dao, Electrochemical impedance spectroscopy of porous electrodes: the eff€ ect of pore size distribution, Electrochim. Acta. 44 (1999) 3513–3519, doi:10.1016/S0013-4686(99)00121-8.

[70] F. Barzegar, A.A. Khaleed, F.U. Ugbo, K.O. Oyeniran, D.Y. Momodu, A. Bello, J.K. Dangbegnon, N. Manyala, Cycling and floating performance of symmetric supercapacitor derived from coconut shell biomass, AIP Adv. 6 (11) (2016), doi:10.1063/1.4967348.

[71] L. Chen, H. Bai, Z. Huang, L. Li, Mechanism investigation and suppression of self-discharge in active electrolyte enhanced supercapacitors, Energy Environ. Sci. 7 (2014) 1750–1759, doi:10.1039/C4EE00002A.